

The cusp plasma imaging detector (CuPID) cubesat observatory: Instrumentation F

Cite as: Rev. Sci. Instrum. **93**, 064504 (2022); <https://doi.org/10.1063/5.0085534>

Submitted: 17 January 2022 • Accepted: 17 May 2022 • Published Online: 08 June 2022

 Emil Atz, Brian Walsh, Connor O'Brien, et al.

COLLECTIONS

F This paper was selected as Featured



View Online



Export Citation



CrossMark

ARTICLES YOU MAY BE INTERESTED IN

[Large dynamic range, high resolution optical heterodyne readout for high velocity slip events](#)

Review of Scientific Instruments **93**, 064503 (2022); <https://doi.org/10.1063/5.0082970>

[Design of the scintillator imaging lens for the neutron imaging system at the 100 kJ-level laser facility](#)

Review of Scientific Instruments **93**, 043303 (2022); <https://doi.org/10.1063/5.0086782>

[A cryogenic torsion balance using a liquid-cryogen free, ultra-low vibration cryostat](#)

Review of Scientific Instruments **93**, 064505 (2022); <https://doi.org/10.1063/5.0089933>

The cusp plasma imaging detector (CuPID) cubesat observatory: Instrumentation

Cite as: Rev. Sci. Instrum. 93, 064504 (2022); doi: 10.1063/5.0085534

Submitted: 17 January 2022 • Accepted: 17 May 2022 •

Published Online: 8 June 2022





View Online



Export Citation



CrossMark

Emil Atz,^{1,a)}  Brian Walsh,¹ Connor O'Brien,¹ Michael Collier,² Ariel Berman,³ Lisa Billingsley,² J. Bernard Blake,³  Jeffery Broll,^{1,b)} Dennis Chornay,² William Crain,³ Thompson Cragwell,^{1,c)} Norman Dobson,² Joseph Kujawski,⁴ Kip Kuntz,⁵ Van Naldoza,¹ Rousseau Nutter,^{1,d)} F. Scott Porter,² David Sibeck,² Kenneth Simms,² Nicholas Thomas,^{2,e)} Drew Turner,^{6,f)} Allan Weatherwax,⁷ Ajmal Yousuff,⁴ and Aleks Zosuls¹

AFFILIATIONS

¹Center for Space Physics, College of Engineering, Boston University, Boston, Massachusetts 02215, USA

²NASA Goddard Space Flight Center, Greenbelt, Maryland 20771, USA

³The Aerospace Corporation, Los Angeles, California 90245, USA

⁴Drexel University, Philadelphia, Pennsylvania 19104, USA

⁵The Henry A. Rowland Department of Physics and Astronomy, Johns Hopkins University, Baltimore, Maryland 21210, USA

⁶Space Exploration Sector, Johns Hopkins Applied Physics Laboratory, Laurel, Maryland 20723, USA

⁷Merrimack College, North Andover, Massachusetts 01845, USA

^{a)}Author to whom correspondence should be addressed: emilatz@bu.edu. Mission website <https://sites.bu.edu/cupid/>

^{b)}Now at: Los Alamos National Lab, Los Alamos, New Mexico, 87545.

^{c)}Now at: Millennium Space Systems, El Segundo, California, 90245.

^{d)}Now at: NASA Goddard Space Flight Center, Greenbelt, Maryland, 20771.

^{e)}Now at: NASA Marshall Space Flight Center Huntsville, Alabama, 35808.

^{f)}Previously at: The Aerospace Corporation, Los Angeles, California, 90245.

ABSTRACT

The Cusp Plasma Imaging Detector (CuPID) CubeSat observatory is a 6U CubeSat designed to observe solar wind charge exchange in magnetospheric cusps to test competing theories of magnetic reconnection at the Earth's magnetopause. The CuPID is equipped with three instruments, namely, a wide field-of-view ($4.6^\circ \times 4.6^\circ$) soft x-ray telescope, a micro-dosimeter suite, and an engineering magnetometer optimized for the science operation. The instrument suite has been tested and calibrated in relevant environments, demonstrating successful design. The testing and calibration of these instruments produced metrics and coefficients that will be used to create the CuPID mission's data product.

© 2022 Author(s). All article content, except where otherwise noted, is licensed under a Creative Commons Attribution (CC BY) license (<http://creativecommons.org/licenses/by/4.0/>). <https://doi.org/10.1063/5.0085534>

I. INTRODUCTION

Magnetic reconnection, a significant term in the magnetospheric energy budget, enables energy to be extracted from the shocked solar wind and deposited it into the Earth's magnetosphere.^{1,2} Once input, this energy drives magnetospheric and ionospheric dynamics.

Despite the importance of reconnection, its macro-scale spatial and temporal properties remain largely unknown. An experimental study of this phenomenon at the magnetopause has predominantly been conducted by *in situ* measurements of magnetic fields, particle populations, and plasma velocities in regions of discontinuity. The instruments on the Cusp Plasma Imaging Detector (CuPID) CubeSat Observatory will be the first to study magnetopause reconnection

with a wide field-of-view (FOV) x-ray telescope in orbit ($4.6^\circ \times 4.6^\circ$, 27.5 cm optic to detector).³

A. Science background

Magnetic reconnection at the Earth's magnetopause is an energy transfer process in which magnetic fields with magnetically trapped plasma break down and reform in a different orientation to transform magnetic energy into kinetic energy. At the Earth's magnetopause, the boundary between the magnetosphere and magnetosheath, the shocked Interplanetary Magnetic Field (IMF) of solar wind, and the Earth's magnetospheric magnetic field frequently reconnect. When reconnection occurs, magnetic topology changes, permitting charged particles from the magnetosheath to travel into the magnetospheric cusps. The opened magnetic field line also gives magnetospheric plasma access to the magnetosheath. The spatial and temporal properties of charged particles in the cusps can therefore provide a proxy for how reconnection occurs at the magnetopause.

Studies of reconnection have long reported conflicting results regarding global conditions of reconnection at the magnetopause. Spatially, reconnection could be occurring in localized patches [fractions of or a few Earth radii (e.g., Refs. 4–7) or extended separators >10 Earth radii (e.g., Refs. 8–10)]. Temporally, observations and modeling have reported that reconnection may be occurring in intermittent bursts (a few minutes) (e.g., 11), continuously (e.g., 12), or continuously at variable rates. Each of these spatial and temporal properties of reconnection will have different particle manifestations in the cusps.

Observations of these precipitating particles in the cusp provide a window to remote sense the processes occurring at the magnetopause. As these particles enter the cusp and upper atmosphere, they interact with neutrals through solar wind charge exchange (SWCX). Soft x rays (0.1–2.0 keV) are released in the process.¹³ Charged particles generating soft x rays can be mapped to the magnetopause where reconnection had initiated.¹⁴ Although other missions, such as Chandra, have observed auroral bremsstrahlung x-ray emissions,¹⁵ the CuPID is a dedicated observatory to monitor SWCX line emissions. Ground-based measurements of the cusp aurora have also been used to study the morphology¹⁶ but are generally limited to a short time period during the year when the cusp footprint is not sun-illuminated. Since soft x rays are not able to penetrate the atmosphere, such a space-based observer is necessary. Spatially, the cusp is typically 2° in latitude^{17,18} and can contain ion dispersions that may or may not have spatial (0.5°) gaps, which are indicators for how magnetopause reconnection occurs [reviewed in the study by Walsh *et al.* (2021) and Pitout and Bogdanova (2021)].^{3,19} This spatial size and the size of the gaps drive the size of the FOV of the x-ray telescope and the angular resolution. Imaging of the x rays created by ion dispersions from inside the cusps with a wide FOV instrument would provide the largest view of magnetopause variations to date.

B. CuPID CubeSat observatory

The CuPID will investigate the properties of Earth's magnetopause magnetic reconnection and provide a major advancement to open questions regarding the spatial and temporal properties of reconnection.

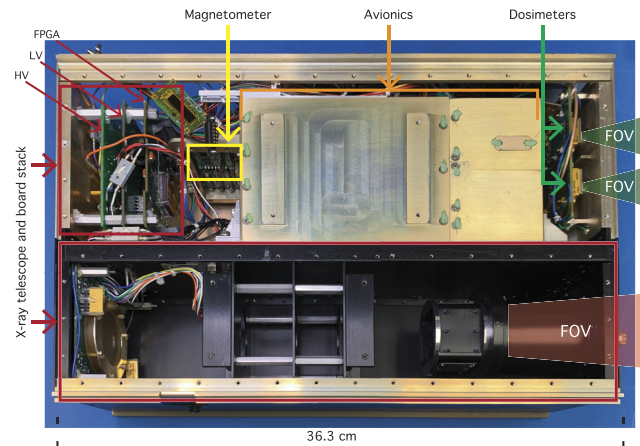


FIG. 1. Telescope optics and detector are enclosed in a light tight portion of the spacecraft (bottom). The x-ray board stack (left: high voltage supply, middle: low voltage supply, and right: Field Programmable Gate Array, FPGA), magnetometer, dosimeter, and avionics occupy the other half of the CubeSat. The FOV of the dosimeter and x-ray telescope are aligned on the same axes.

The CuPID is equipped with three instruments, namely, a wide field-of-view ($4.6^\circ \times 4.6^\circ$) soft x-ray imager, a collimated micro-dosimeter suite, and a body mounted magnetometer. The x-ray telescope will image photon emission from SWCX, while the dosimeter measures precipitating energetic particles. The design of these instruments is unique and leverages the full platform of the CubeSat design with integrated structures to minimize the weight and size. The design allows the telescope to operate in a 6U CubeSat structure (Fig. 1). The telescope occupies approximately one-half of the chassis, and the x-ray electronic boards, magnetometer, dosimeter, and avionics occupy the other. Due to the optical nature of the mission, the spacecraft is three axis stabilized to provide accurate pointing in regions of magnetic reconnection interest. The CuPID was launched on September 27, 2021, from Vandenberg Space Force Base into a near sun synchronous orbit at 550 km with an inclination of 97.6° and a right angle of the ascending node (RAAN) of 338° , putting the sun-side of the CuPID's orbit plane just before local noon. Since the cusp is fixed near local noon, a RAAN, which allows for the spacecraft to pass near this region for some dipole tilts, is important for observations.

During science operation, the CuPID will point the co-aligned x-ray telescope and dosimeter zenith (radially outward from the surface of the Earth) to image along the cusp field lines. The high inclination orbit of the CuPID will frequently track the spacecraft directly through the cusps depending on the position of the constantly moving cusps. Zenith pointing is necessary to limit emissions from lower altitudes.

II. CUPID SCIENCE INSTRUMENTATION

CuPID's instrument requirements are driven by the mission science goals. The goal for the x-ray instrument is to identify gaps in ion dispersions in the cusp. The spacecraft bus has a pointing control and knowledge requirement of 0.25° due to the optical nature

of the mission. The FOV of the x-ray telescope must be greater than 4 circular to capture the cusp from low Earth orbit. A resolution of 0.25° is necessary to define the spatial features of soft x-ray emissions in the cusp. The structure of the x-ray telescope requires a three-bounce “light tight” assembly such that stray external light cannot directly excite the detector. The dosimeter must measure precipitating particles that can contaminate x-ray images; therefore, it is co-aligned with the x-ray telescope. To measure the low pitch angle, precipitating particles when pointing zenith, the FOV of the dosimeter less than 45° is required. The magnetometer, initially only required for attitude determination, was characterized to enable the science team to identify the dynamics of low altitude auroral current sheets through magnetic field reversals, which are often greater than 100 nT.

Sections II A–II C separately describe each of the instruments in detail and include experiments conducted to calibrate and quantify their performance.

A. Soft x-ray telescope

X-ray telescope optics must use grazing incidence reflection to focus photons as opposed to refraction in conventional visible light optics. A comparison of x-ray instruments is detailed in Table I. One option of x-ray optics, Wolter optics (types I, II, and III), uses circular nested mirrors to reflect x rays toward the optical axis.²⁰ To date, the most common x-ray optics on a satellite platform are Wolter type I optics. Wolter type I optics are typically used for astrophysical missions where science targets have small angular sizes in the sky. A number of past x-ray observatories, such as Chandra, ROSAT, Suzaku, Swift, and XMM Newton, have relied on this focusing method. Instruments with Wolter optics trend toward larger diameters and longer focal lengths to increase the collecting area and resolution for their astrophysical missions.

Another method of x-ray imaging is with the use of a coded aperture. Coded aperture imagers utilize the principles of single pin-hole cameras but with a well-calibrated array of pixel apertures.²¹ Instead of redirecting photons to a focused point, coded apertures restrict incident photons only to those that pass directly through the aperture. The FOV of a coded aperture instrument is defined by the aperture and detector size, as well as the spacing between them. Coded aperture instruments have been utilized on celestially

targeted missions, such as INTEGRAL,²² SWIFT,²³ and SuperAGILE,²⁴ observing gamma and hard x-ray photons. The Earth observing instrument, the modular x- and gamma-ray sensor on board the International Space Station, also uses a coded aperture imager with a FOV of $80^\circ \times 80^\circ$.²⁵ The CubeSat AEPEX, currently under development, will operate a $90^\circ \times 90^\circ$ FOV Earth observing coded aperture instrument for auroral observations.²⁶ Although coded aperture instruments provide an exceptional FOV, the instruments require large computational resources to reconstruct the image. Additionally, these imagers require a significantly strong target source to maintain a high signal to noise ratio with only a 50% open area.^{27,28}

The third option, micro-pore optics (MPO) also known as lobster eye optics, utilizes a biology mimicking technique to focus x rays with small square channels aligned normal to a spherical surface. A number of theoretical and experimental studies have characterized this x-ray imaging technique.^{29–33} MPO based instruments permit a much lower size and mass with a larger FOV in comparison to Wolter I optics. MPOs are becoming more prevalent in planetary and heliophysics missions because of the access to a larger FOV (multiple degrees rather than fractions of a degree).³⁴

A number of missions have flown with MPOs in recent years or are in development to fly such optics in the near future. The first flight of lobster-eye focusing elements was the DXL/STORM (Diffuse X-ray emission from the Local galaxy/The Sheath Transport Observer for the Redistribution of Mass) instrument that flew on a sounding rocket from White Sands, New Mexico, in 2012.³⁵ As the secondary instrument on the DXL mission, the STORM instrument raised the technology readiness level of lobster eye optics and tracked a transient feature through the sky.³⁶ Progress has been made rapidly since this flight. Recently, the Longxia Yan 1 lobster eye x-ray satellite has also been launched into low Earth orbit. The planetary mission BepiColombo carries MIXS (Mercury Imaging X-ray Spectrometer) instruments, which combines two telescopes, one with MPOs and one utilizing Wolter optics for x rays focusing at Mercury. BepiColombo’s instruments have survived launch and endured near Earth calibrations but are awaiting arrival at Mercury.³⁷ Looking forward, the Lunar Environment heliophysics X-ray Imager (LEXI) uses an array of nine MPOs and is scheduled for deployment on the lunar surface in 2024 as part of NASA’s Commercial Lunar Payload Services (CLPS) program.

TABLE I. Comparison of current and future x-ray instruments.

Mission/Instrument	Launch Year	Optic Type	FOV	Focal Length (cm)
CuPID	2021	MPO	4.6°	27.5
DXL/STORM ^{36,38}	2012	MPO	$6^\circ \times 3^\circ$	37.5
LEXI	2024 ^a	MPO	9.2°	37.5
SMILE/SXI ³⁹	2024 ^a	MPO	$15.6^\circ \times 27.3^\circ$	30
BepiColombo/MIXS-C ^{40,41}	2008	MPO	10.4°	55
ROSAT ⁴²	1990	Wolter 1	0.6°	240
Suzaku/XRT ⁴³	2005	Wolter 1	0.25°	475
SWIFT/XRT ⁴⁴	2004	Wolter 1	0.4°	350
XMM-Newton/EPIC ⁴⁵	1999	Wolter 1	0.5°	750
Chandra ⁴⁶	1999	Wolter 1	0.267°	1000

^aScheduled launches.

The ESA-CAS SMILE mission will also carry an array of 32 MPOs and is planned to launch in 2024.

The CuPID soft x-ray telescope detector and signal chain electronics are refurbished hardware that flew on a sub-orbital sounding rocket mission, the Diffuse X-ray emission from the Local Galaxy (DXL-2) as a secondary payload.^{47,48} The progression from the sounding rocket to CubeSat has been applied to small scale soft x-ray instruments before. A notable mission is the Amptek X123-SDD soft x-ray spectrometer flown on two solar dynamics observatory/EUV variability experiment sounding rocket missions in 2012 and 2013.⁴⁹ From these flights, the instrument was modified for successful operation in the MinXSS CubeSat.⁵⁰

The CuPID's zenith pointing telescope targets the photons from SWCX in the cusp. The spectrum is a series of line emissions ranging from several hundred eV to over 1 keV (see the spectrum in the study by Walsh *et al.*, 2021³). For the science objectives of the CuPID, all the lines in this range will be integrated for a single signal. The modeling of the cusp provides an expected few hundred counts/s in the instrument during a cusp pass (<2 min). Instrument count rates are dependent on background emissions (cosmic x rays, near Earth extreme UV, and energetic particle contamination) and the signal from the cusp and magnetosheath. During data processing, the position of signals on the CuPID is converted to a right ascension and declination angles that are used to create an exposure map of CuPID's observations in orbit. The cosmic soft x-ray background has been well mapped and can be removed.⁵¹

Figure 2 presents the modeled signal from the cusp monitored by the CuPID for both (a) single extended ion dispersion and (b) multiple detached reconnection sites along the magnetopause, causing multiple dispersions with gaps or discontinuities in local time. X-ray emissions generated by charge exchange are frequently modeled using data from neutral and MHD models combined with knowledge of efficiencies from atomic priorities and collisions as described in the study by Kuntz *et al.* (2015),⁵² Sibeck *et al.* (2018),⁴⁸ and Connor *et al.* (2021).⁵³ In the current model, the neutral model described by Bailey and Gruntman (2011)⁵⁴ was combined with an analytic model for the cusp plasma density based on the study by Walsh *et al.* (2016).⁵⁵ A galactic background component of 20 keV/(cm² · s · sr) was included, which represents an average value from the ROSAT All Sky Survey in the 1/4 keV band. The total modeled signal is then passed through instrument efficiency and response function to generate counts/second/pixel. Finally, Poisson noise is added. Since all counts are telemetered to the ground, the pixel size is user defined during post-analysis. In these plots, a pixel size of 0.5° was selected.

1. Mechanical and optical design

The layout of the telescope is presented in Fig. 3. The mechanical components are all black anodized 6061 aluminum except for one iridite aluminum 6061 chassis rail. Incident photons enter the spacecraft through a 6 cm diameter aperture in a chassis component. Photons entering from an angle outside the FOV are blocked by the sun shade, a 6.9 cm long tapered cylindrical element designed to shield the instrument from photons more than 35° off axis. Photons with incident angles such that they pass the sun shade then encounter the optic filter. The filter, made of 30.7 nm aluminum on top of 217.9 nm polyimide, is designed to limit visible and UV photons and charged particle contamination.³⁶ The filter

Cusp SWCX Emission with Poisson Noise

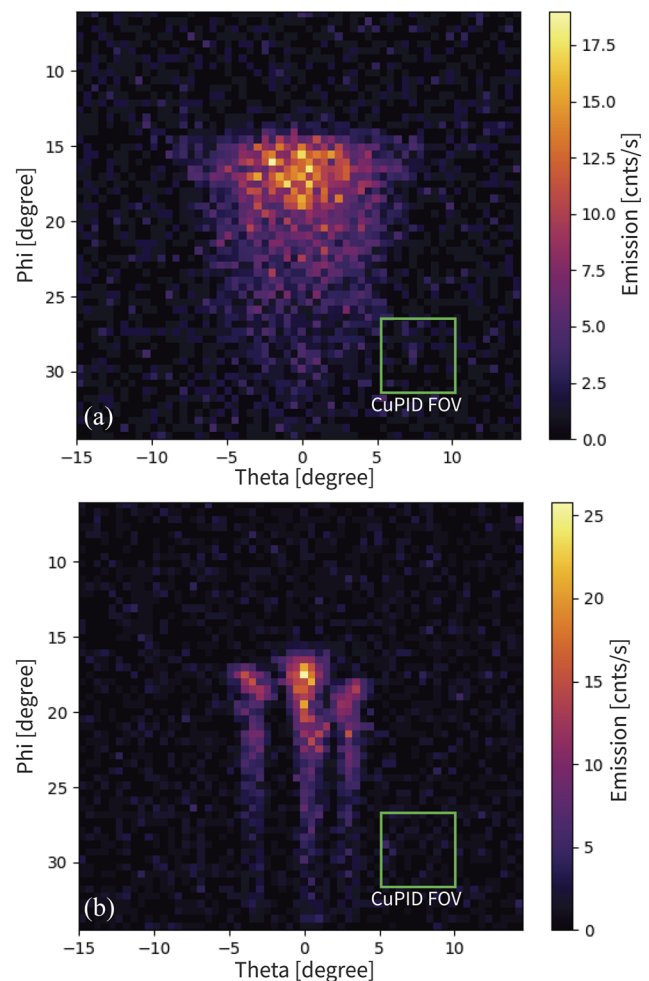


FIG. 2. Modeled count rates in the cusp from solar wind charge exchange during nominal solar wind conditions and different input ion dispersions. As the CuPID scans through the sky, it will sweep through the cusp. (a) A single continuous enhancement is seen corresponding to a single continuous reconnecting separator at the dayside magnetopause. (b) Patches are observed corresponding to multiple discontinuous reconnecting separators, leading to multiple ion dispersions in the cusp occurring, rather than a single ion dispersion turning on and off.

is mounted on top of the convex surface of the MPO by the filter manufacturer.

The 4 cm square MPO is 1 mm thick and composed of square 20 μm lead glass channels with 6 μm walls, resulting in a 60% open area. The width to the length ratio (W/L) of a pore is $\frac{1}{50}$. The array of pores is slumped over a sphere to align the walls normal to the spherical curve. The optic's radius of curvature of 550 mm focuses photons from infinity to a point half the radius of curvature (27.5 cm). The optic was produced by Photonis France SAS.

Photons encountering the optic plane could have several paths. Photons that pass unaffected by the pores directly excite the detector without focusing. Photons that undergo one reflection in the optic

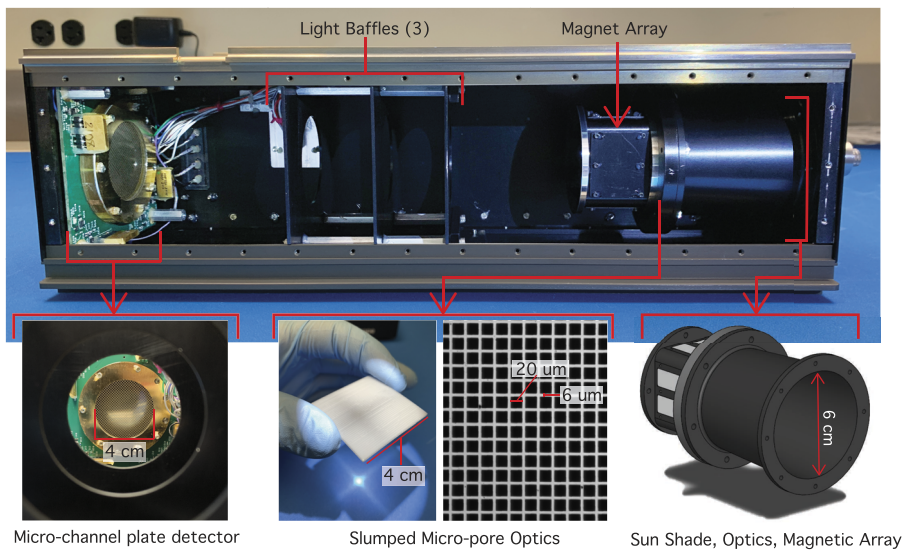


FIG. 3. Layout of the CuPID x-ray telescope. The sunshade limits external light from the instrument. The 1 mm thick optic with 20 μm pores focuses x rays. A magnet array behind the optic sweeps energetic particles away from the optical axis. Light baffles prevent internal fluorescence from exciting the detector. The 4 cm diameter micro-channel plate (MCP) observes photon position and timing.

form the arms of the point spread function (PSF) shown later in Fig. 11. Photons that reflect twice off orthogonal faces in the optic form the center spot of the point spread function.⁴⁸ Focused photons comprise 17%–25% of the PSF.

Immediately after the MPO is an array of eight neodymium magnets, arranged two to a side of a square structure to create a quadrupole. This geometry provides a strong local field, but the higher order minimizes the field strength farther away from the array. These magnets deflect charged particles that pass through the optics away from the optical axis and could contaminate detector images. Although charged particles are deflected by the magnetic field, photons pass unaffected. The now focused photon travels through a set of three unique light baffles, which are used to prevent any external stray photons and internal fluorescence resulting from energetic particle interactions inside the telescope bay from exciting the detector. If excited by incident energetic particles, the aluminum 6061 structure of the instrument and spacecraft could fluoresce and emit K-alpha x rays from magnesium (1.25 keV), aluminum (1.49 keV), and silicon (1.74 keV), as well as others above 2 keV, outside the effective quantum efficiency of the detector. The x ray then reaches the micro-channel plate (MCP) detector.

2. Signal chain and detection system

The steps described in this section can be followed in the block diagram (Fig. 4). The photon, now through the mechanical/optical parts of the telescope, excites the circular MCP. The MCP, manufactured by Photonis, is 4 cm in diameter, with two plates assembled in a chevron pattern. The channels are 25 μm in diameter with a bias angle of 8°. The MCP is coated with potassium bromide (KBr) to improve soft x-ray sensitivity.⁵⁶ Photons that impact the MCP liberate electrons, which subsequently liberate more as the electron cloud is swept through the MCP. Electrons are swept by a strong electric field generated by a ground mesh and high voltage (HV) board on either side of the MCP (see the mesh in front of the MCP in Fig. 3). Behind the MCP is the anode board. The anode board is a wedge and strip detector that produces position data.^{57,58} The custom-built

wedge and strip anode layout is a 4 cm square layout with four channels, two wedges, and two strips where each unit is 0.029 inches wide.

The electron cloud from the MCP deposits charge into these channels on the anode, and the signals are amplified by four charge sensitive pre-amplifiers. The Amptek A111 pre-amplifiers produce signals between 1 and 4.5 V, corresponding to the amount of charge deposited into each channel of the wedge and strip. These voltages are later converted to an X and Y position on the MCP. Valid signals are determined as those within 2.1 and 3.3 V. Voltages outside this range have a non-physical meaning, such as lying outside of the MCP area once converted to an X and Y position. Further discussion of valid signals is in Sec. II A 3 a.

The MCP/anode detector and x-ray board stack are structurally separated in the chassis due to space constraints. Telemetry and power between the MCP and the board stack are routed through a bulkhead connector in the center of the spacecraft (see Fig. 1 for the layout and Fig. 3 for bulkhead wiring). The ProASIC3 FPGA in the board stack reads the four channels of telemetry, applies any user commanded thresholds, adds a mission elapsed time tag to the data, and passes it upstream to the spacecraft flight computer. The FPGA also produces housekeeping telemetry. This telemetry contains a time tag, as well as HV setting and temperature, and event counts.

MCP telemetry is converted to the position on the detector using a centroid finding relationship between the charges deposited in the four channels.⁵⁹ The charge in one wedge or strip is divided by the total charge deposited onto the pair of wedges (X) or pair of strips (Y), as seen in Eq. (1). On-board data processing uses this equation to cut each telemetry item from four voltages to two positions. The origin of the data is shifted to (0, 0) by subtracting 0.5. This equation results in a unitless number that is converted to a plate scale using results from an experiment on the MCP,

$$\begin{aligned} X &= [x_0/(x_0 + x_1)] - 0.5, \\ Y &= [y_0/(y_0 + y_1)] - 0.5. \end{aligned} \quad (1)$$

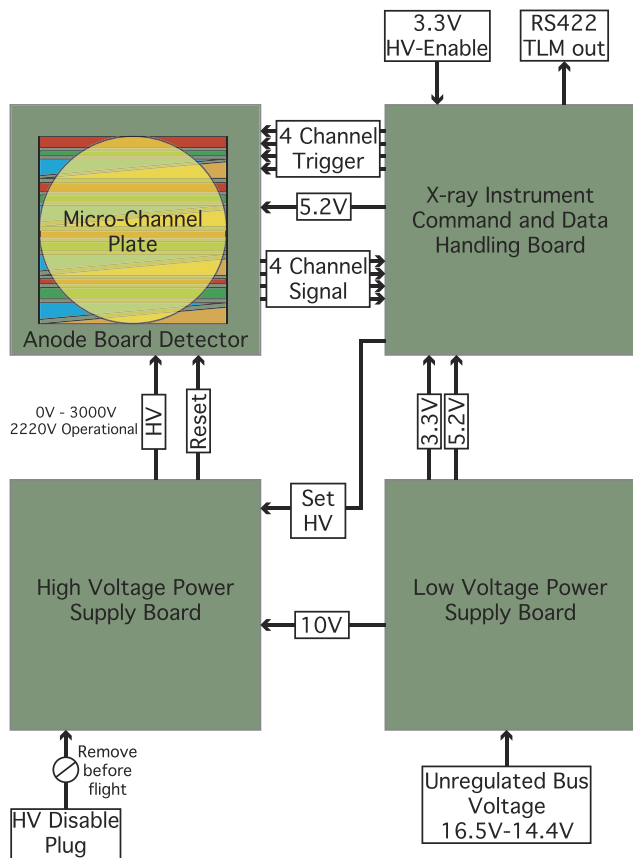


FIG. 4. Block diagram of the x-ray telescope electronics. The low voltage board (bottom right) takes supply from the spacecraft bus and powers the telescope. The ProASIC3 FPGA on the command and data handling board (top right) manages commands and telemetry. The HV board (bottom left), with a power supply of 3 kV, biases the detector system. The MCP and the wedge and strip detector (top left, example wedge and strip array) provide position sensing data of incident photons to the FPGA.

The MCP detector does not have the ability to distinguish photon energy. Instead, the x-ray telescope is an event counter and records the position and timing of each photon. Images are not created on the spacecraft. Instead, images are created on the ground, allowing the user to define the integration period and pixel geometry to best suit the data.

The x-ray instrument data are stored in three files on-board CuPID. First are 10 second count rates and active x-ray file numbers in a combined science data and spacecraft housekeeping file. This summary file is downloaded each pass to determine the areas of interest. The file size is large enough to record one day. Second is a complete data stream from the instrument, including all instrument housekeeping data and time-tagged, four MCP output voltages. This file, labeled as x-ray burst data, is downloaded only if needed because it contains only 36 000 entries split between instrument housekeeping and science data. The third file, named x-ray fast, has 57 600 processed science data points. These data are the time-tagged X and Y positions of valid photons on the MCP. The summary file

aids an operator in determining which x-ray fast file to download. Further discussion of the complete spacecraft data process is found in the study by Walsh *et al.* (2021).³

3. Calibration and qualification

Calibration of the x-ray telescope involved testing of individual elements and testing of the fully integrated CubeSat instrument. Physical experiments with the x-ray telescope require high vacuum and were conducted under vacuum with pressures less than 5×10^{-6} torr.

a. Detector The relationship between the MCP output voltages to a distance measurement on the detector and detector linearity was calibrated using a thin metal mask. The grid mask with 0.1 in. diameter holes spaced 0.3 in. apart was mounted on standoffs less than $\frac{1}{2}$ cm in front of the MCP. An Iron 55 (Fe55) source, producing 5.9 keV x rays, was mounted opposite, near where the optic would mount. The experiment layout is shown in Fig. 5(a). The instrument collected data for over 12 hours, and the result is plotted in Fig. 5(b). With a known size and spacing of the mask holes, a relationship between MCP voltage and plate scale is generated. This result showed a shift in the data, caused by electrical differences in the channels. The data were reoriented using a basis transformation with the result shown in Fig. 5(c). The size of the MCP detector, shown with the white lines, is defined from the distance between the dots and the edge of the grid image. Three additional mask designs were tested, which aided in the basis transformation and defined the instrument axes in CuPID's spacecraft vehicle axes, which is essential for pointing knowledge on orbit.

The detector background is highly dependent on pressure and contaminants in the detection system. Background counts arrive at a Poisson arrival rate, where the timing between events is random. Background counts on the MCP produce voltages that are lower or higher than the valid count voltage range (2.1–3.3 V). The valid count voltage range is a configurable parameter. After environmental testing, an increase in background count rates was found to be caused by dislodged contaminants in the instrument. The instrument spent five weeks under vacuum to decrease the background count rates by out-gassing the contaminants. The decrease in the background is shown in Fig. 6(b). Although the raw count rate is high, the valid count rate is low. The instrument responds with weak signals to non-photon excitation, such as off-gassing contamination on the MCP. The instrument background delivered to the launch vehicle is shown in Fig. 6(a). Background rates will continue to decrease on orbit. The valid signal from cusp observations is expected to be greater than a few hundred counts per second; therefore, the signal (300–400/s) to noise (12/s at delivery) ratio is high during cusp observations. Early on orbit commissioning will include a flat field image of the dark night side Earth to quantify the background counts after launch.

As described in Sec. II A 2, the detector of the x-ray instrument uses HV to sweep electrons from the MCP to the anode board. This HV is configurable. The HV setting was optimized experimentally and set to 2220 V for the beginning of the mission. The experiment used a beam line with an aluminum target to fluoresce aluminum $\kappa\alpha$ 1.49 keV x-rays toward the detector with a small grid mask similar to that shown in Fig. 5. Through operations that mimicked the

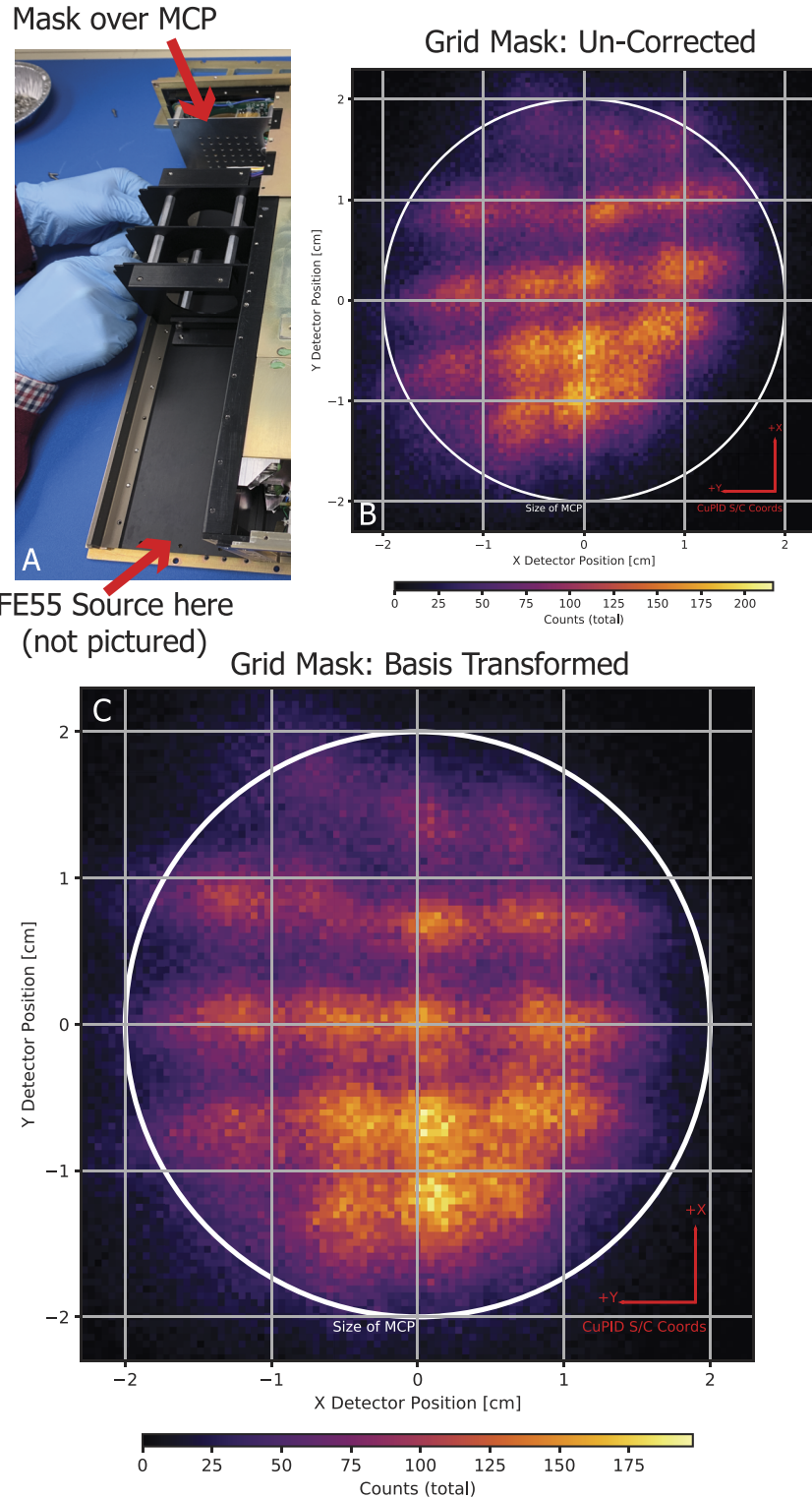


FIG. 5. Calibration of the MCP detector using a grid mask: (a) assembly of the experiment in the flight chassis. The radiation source is not shown. (b/c) Plots of the data as uncorrected and corrected 2D histograms. X- and Y-axes indicate the detector position in cm as determined by this experiment. Colors indicate the number of counts inside the bins. One bin represents 0.46 mm on the detector. CuPID's vehicle axes are shown in red.

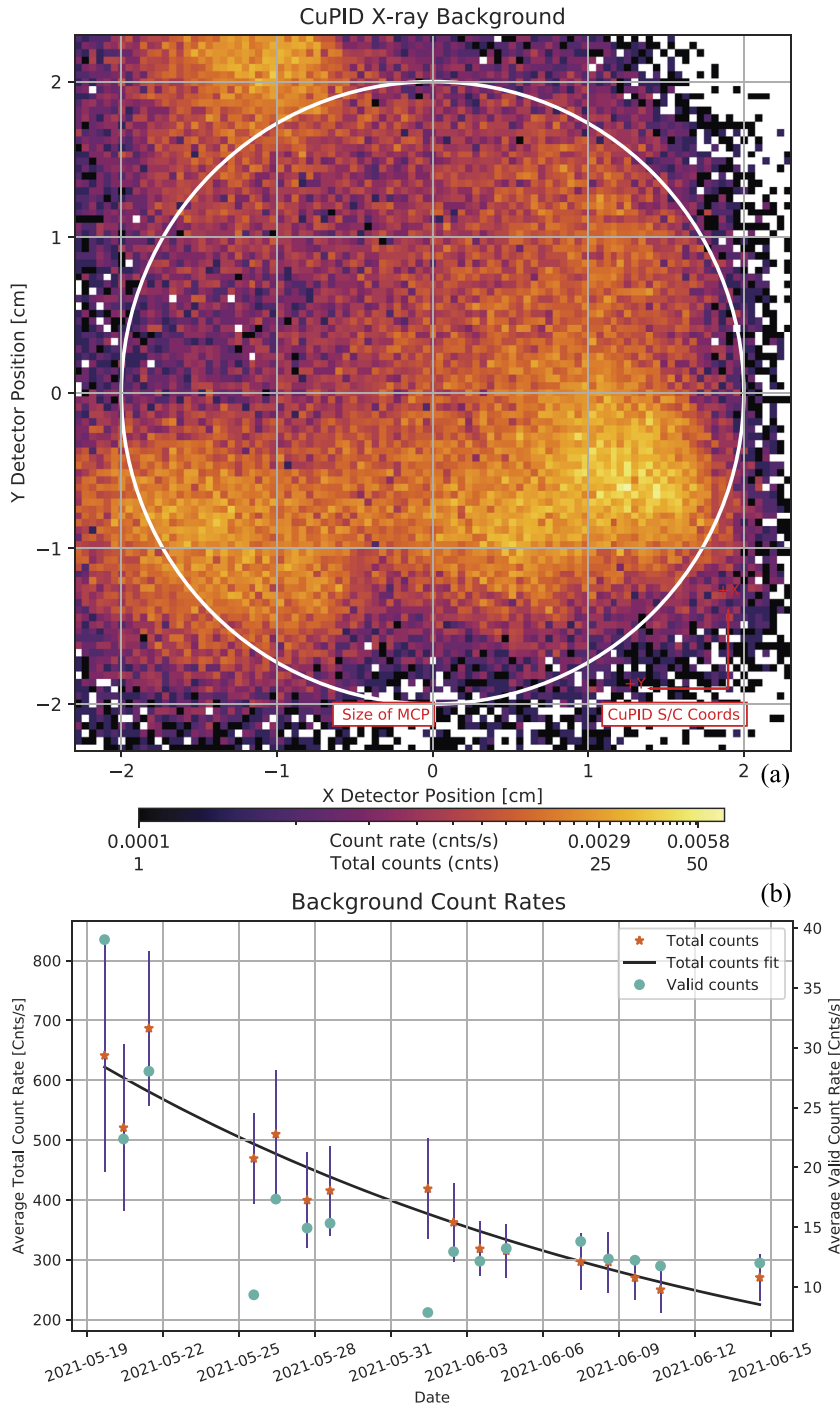


FIG. 6. CuPID's x-ray MCP background measurements: (a) background image of the MCP as delivered to the launch vehicle and (b) background count rates of the MCP after environmental testing decrease with time under vacuum.

on-orbit commissioning phase of the instrument, the HV was stepped up and >20 minutes of counts were collected at each step.

Average count rates are plotted in Fig. 7. These count rates include the x-rays from the beam line and background noise counts. At the sampling of the 2240 V data point, a pressure increase in

the chamber occurred, causing the increase in the count rate. The pressure increase did not bring the chamber pressure above 2×10^{-6} torr, so the experiment proceeded. 2220 V was selected as operational because the count rate began to linearize, and increasing the voltage would not significantly benefit the result.

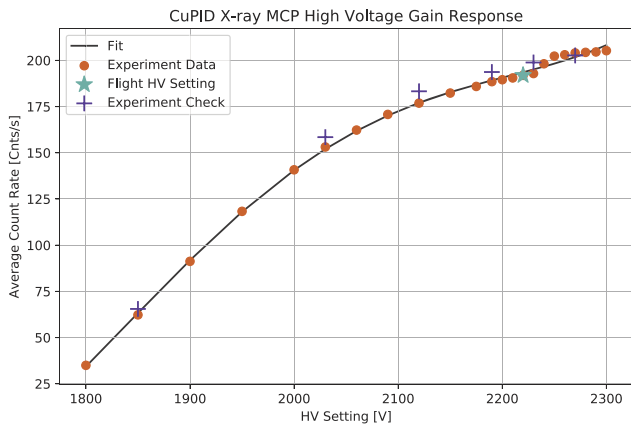


FIG. 7. Gain curve of the CuPID's MCP comparing commanded HV setting to the MCP count rate. Experiment ramped up HV to 2300 V. Experiment data: averages of 20 min of count rate at HV setting and experiment check: a ramp down of HV and 10 min averages. The flight setting for the CuPID is 2220 V shown as the teal star.

b. Optics The MCP responds to any incident radiation, and energetic particle contamination can be problematic. The sweeper magnet array of the CuPID, mounted behind the optics, creates a strong magnetic field to redirect particles that pass the optic. The 8 neodymium bar magnets in the array are oriented to create a quadrupole and minimize the far field to limit the impact on the internal magnetometer of the CuPID. The impact on the magnetometer was determined to be 23 000 nT in magnitude. This uniform field is easily removed for on-orbit measurements. The permanent magnets vary on the order of 1%–2% over the course of 10 years per the vendor characterization. Over the CuPID mission, this is on the order of 0.1%. Figure 8(a) presents the measurements of the magnetic field from 77 points distributed around the array, taken in a plane perpendicular to the optical axis. The four nodes of the quadrupole field can be seen. The orientation of the quadrupole is

shown with the vectors. Figure 8(b) shows a slice of the contour at $X = 0$ and $Y = 0$. The magnetic field strength reaches above 0.04 Tesla.

The electron suppression of the optic system was measured with a Nickel 63 radiation source (Ni63: β -spectrum, 67 keV maximum with 17 keV average). Figure 8(c) reports suppression results from the experiment. The magnets suppress the Ni63 electrons by a factor of 7. The optics, with the aluminum/polyimide optic filter described in Sec. II A 3 1 and as described in the study by Collier *et al.* (2015), suppress the electron flux by a factor of 100. Additionally, protons at 10 keV are suppressed by a factor of 10^5 by the optic and filter.³⁶ Energetic particles in the cusp can add to the instrument background. Electrons in the cusp are lower than a few hundred eV and easily excluded by the optic or magnetic sweeper magnets. The peak ion flux in the cusp is near 3 keV and thus suppressed significantly by the optic. Above 10 keV, measurements from the cluster mission found the ion energy flux to be typically lower than 10^6 eV/cm²-s-sr-eV.¹⁷ The optic area (16 cm²), solid angle (0.006 sr), and optic transmission (10^{-5}) of the CuPID when combined with this energy flux result in count rates less than one count every 50 cusp crossings, effectively 0.0001/s.

The FOV of the telescope was modeled with a custom-built MPO ray-tracing code developed by team members at Johns Hopkins University. The optic is modeled by assuming that each pore is fully filled with rays incident at some angle to the optical axis. The reflectivity is a function of energy and angle of incidence. Since the x rays of interest have energies <2 keV, x rays striking the pore walls at nearly normal incidence are assumed to be absorbed. For a given incidence angle with respect to the pore axis, a ray may be reflected n or $n + 1$ times in each dimension; for a perfect pore, there are exactly four different possibilities for the output ray direction, each with a different attenuation due to the dependence of the reflectivity on the angle of incidence. The vignetting function, as a function of energy, is the throughput as a function of the angle of incidence with respect to the optical axis (Fig. 9).

Modeling allows testing above and below the expected soft x-ray spectrum the CuPID can observe. Transmission through the

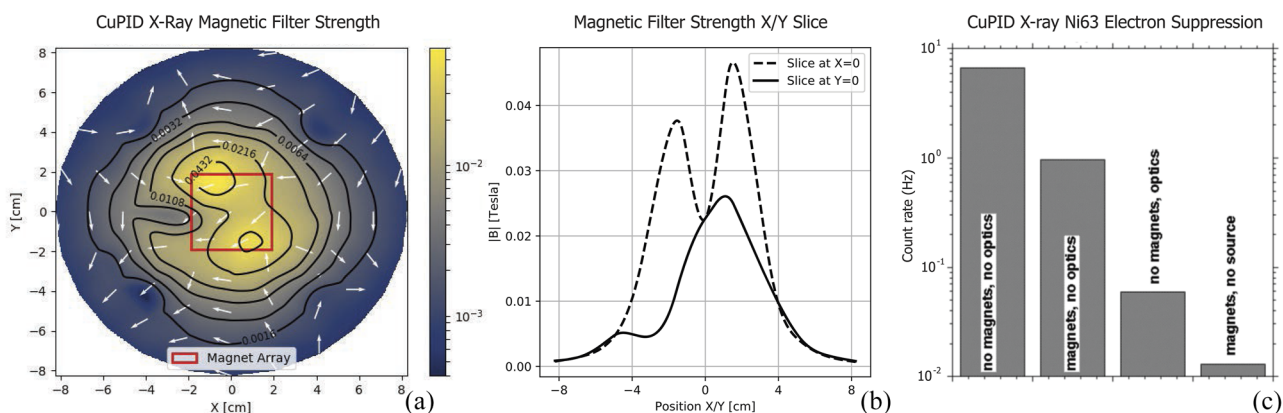


FIG. 8. CuPID's sweeper magnet array strength. (a) Contour plot of the field strength generated from point measurements. The magnet array size is shown as the red square. (0, 0) is located at the center of the magnet array. (b) Slice of the field strength along $X = 0$ and $Y = 0$. (c) Electron rejection measurements from the optic system using an Ni63 radiation source. Background counts are "magnets, no source," and incident radiation from the Ni63 source is "no magnets, no optics."

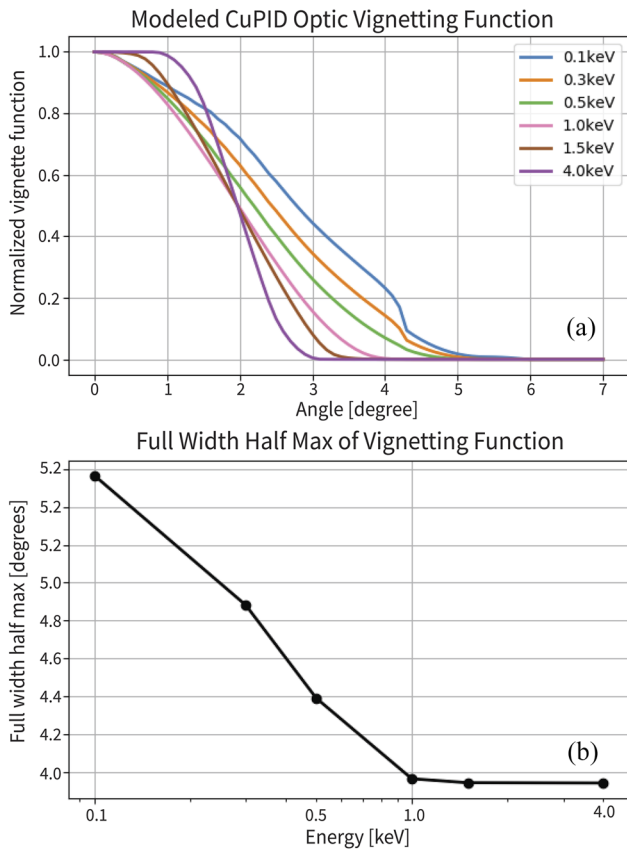


FIG. 9. (a) Vignetting function or FOV of the CuPID as modeled with varying energies. The X-axis of the plot is the angle off of the optical axis of the telescope. (b) FWHM of the vignetting function at each energy modeled.

filter is low below 0.2 keV, and the detector efficiency decreases dramatically above 1 keV. The total effective area of the CuPID x-ray telescope was determined through a combination of manufacturer measurements and modeled values. Figure 10 reports the total effective area of the CuPID, with the targeted energy band from 0.1 to 2 keV. From the total effective area and modeled vignetting function, the FOV of the CuPID is defined as $4.6^\circ \times 4.6^\circ$.

The PSF of CuPID's optic was measured at the Goddard Space Flight Center 100 m beamline. The beam line used a soft x-ray Manson source powered at 10 kV and 1 mA with an aluminum target to produce 1.49 keV x rays. At 100 m, the source size is unresolved for MPOs. The optic was mounted at 275 mm from a CCD detector. The 26 mm by 26 mm CCD detector output counts in 0.02 mm pixels with a 120 s exposure. Figure 11 shows the PSF with a bin sized 0.46 mm, comparable to the bins of CuPID's MCP in Figs. 5(b), 5(c) and 6(a). The FWHM (full width half maximum) of the PSF was calculated by fitting a 2D-Gaussian to the data. The optic's PSF FWHM is 9.2 arcmin in the X-axis and 22.1 arcmin in the Y-axis, with an average of 15.65 arcmin. The position sensing of the MCP is finer than the PSF size; therefore, the PSF drives the angular resolution of the instrument. The double arms of the PSF are due to the

suboptimal optic and detector spacing. The optic purchased was ordered at a radius of 55 cm for a 27.5 cm focus but would perform better at a slightly longer distance because the actual slumped radius does not match perfectly to the ordered one. After this discovery, modifications to the structure that mounts the detector/optic were not possible. Additionally, aberrations in the optic pore structure, such as pore shear and pore bundle misalignment, can subtract from the performance of the optic, as seen by the periodicity along the top and bottom PSF arms.³³

The percent of focused light vs total light is 8.7% with 3.2% inside the FWHM of the PSF. These photons are focused by an odd number of reflections off orthogonal pore walls, focusing into the center of the PSF, or pass through the center pores not reflected. Reflectivity decreases as photon energy increases, and the 1.49 keV photons used in the experiment are on the higher end of CuPID's capability. This, in addition to the focus distance and optic aberrations, causes the lower than expected (20%) focused light.

CuPID mission is not significantly affected by these results. The wider than expected PSF slightly impairs the as-built instrument's expected resolution. The spatial resolution of the CuPID is motivated by the need to resolve gaps in cusp ion dispersions ($\sim 0.5^\circ$), which is still satisfied by the asymmetric imaging resolution. The lower than expected focused light percentage decreases the throughput of the instrument, which will only require longer exposures during data processing.

B. Micro-dosimeter instrument

Energetic particle dosimeters are used on satellites to monitor the radiation dose to satellite components. Dosimeter instruments vary in size, weight, and power metrics. A notable mission that operated a dosimeter instrument is the Van Allen Probes and its Engineering Radiation Monitor (ERM).⁶⁰ The ERM is an array of 8 dosimeters with varying shielding to measure a dose depth curve during the duration of the mission.⁶¹ Past and present CubeSats have also operated dosimeters, or more advanced small scale particle telescope instruments, produced significant scientific results,⁶²⁻⁷¹ and advanced the community's instrument development knowledge (e.g., Ref. 72). A comparison of these instruments is shown in Table II. These CubeSat particle instruments vary greatly in design and capability.⁷³⁻⁷⁹ For efficient use from a CubeSat platform, an instrument needs to be of low volume, power, and mass. Depending on the requirements of the science mission, dosimeters excel in CubeSats because of their small size and power requirements as compared to larger particle telescopes that have particle energy resolution.

For the CuPID mission, the dosimeters are necessary to monitor the energetic particles that can contaminate the x-ray telescope images. Energetic charged particles (>50 keV) have access to the low altitude magnetosphere in several regions including the south Atlantic anomaly, as well as at high latitudes where magnetic field lines converge at the foot points of the radiation belts and auroral regions. Past x-ray missions have worked hard to quantify the presence of energetic charged particles that can excite the detector and cause a background for soft x-ray measurements.⁸⁰ Since the primary science target of the CuPID, the magnetospheric cusp, is adjacent to a region with closed magnetic field lines that can contain high fluxes of energetic particles, it is important for the mission

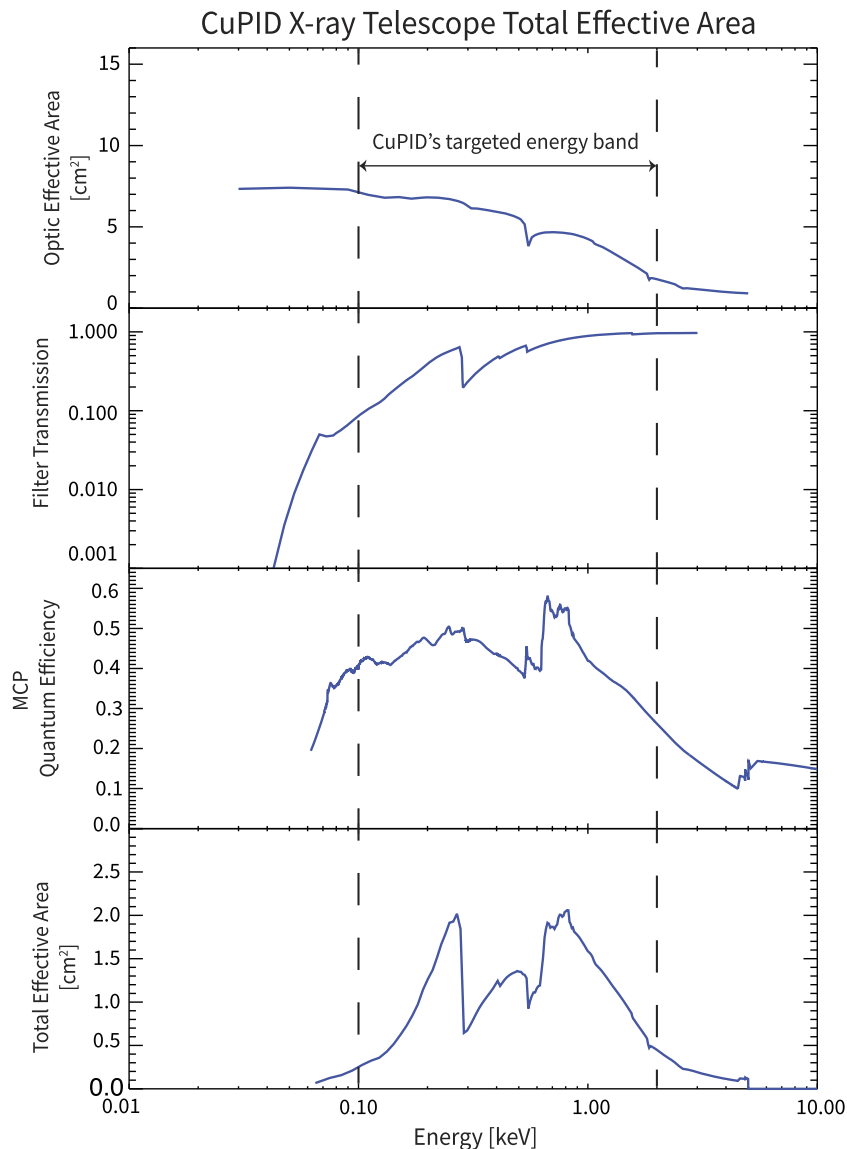


FIG. 10. Elements used to calculate the total effective area of the CuPID x-ray telescope. From top to bottom: modeled effective area of the optic, transmission rates through the aluminum/polyimide filter, quantum efficiency of the MCP, and total effective area.

to quantify time periods when fluxes are high both as a background monitor and to help identify when the CuPID is in the cusp. Secondary science of monitoring trends in precipitation of radiation belt particles in conjunction with other observing platforms is also possible.

The CuPID micro-dosimeter suite is a small scale particle instrument developed by The Aerospace Corporation to measure energetic ions and electrons. The instrument uses detectors manufactured by Teledyne, modified for the CuPID science target, and is based on similar instruments developed by The Aerospace Corporation. The instrument contains two detectors, Dosimeter A (Dos A) and Dosimeter B (Dos B).

1. Mechanical design

The dosimeter instrument is composed of a single circuit board mounted with 5/8 inch standoffs to a chassis component of the spacecraft with machined apertures for each detector. The FOV of the suite is co-aligned with the x-ray telescope, as shown in Fig. 1. Optimized for the small form-factor of a CubeSat, the circuit board is an “L” shape to accommodate a GPS (Global Positioning System) antenna that is also located on the structural face. Excluding the chassis component and standoffs, the dosimeter suite has a mass of 70 g. The detectors are collimated by precisely machined holes, 0.26 in. in diameter with a 45° chamfered backside to prevent

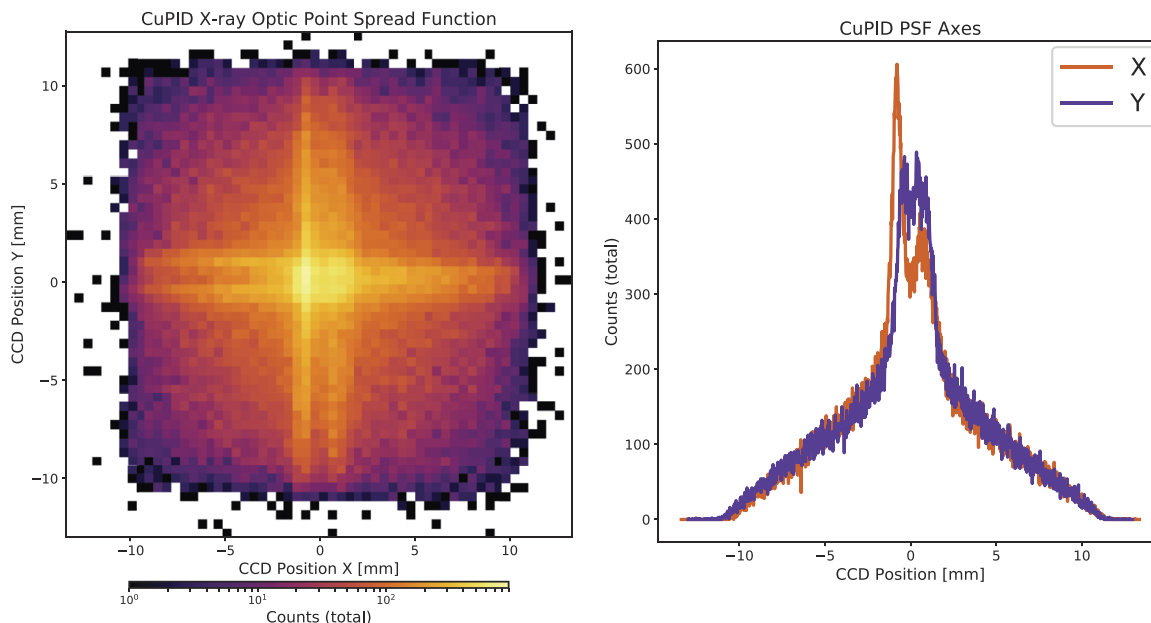


FIG. 11. Optic point spread function of the CuPID and summation of counts along each axis.

energetic particles from interacting with the edge material. In addition, although the detectors are designed to be separated far enough apart to prevent cross-contamination from particles that enter the aperture at highly oblique angles, a metal separator was included between the detectors to prevent this effect. Figure 12 shows how the dosimeter is assembled with the endcap structure of the CubeSat.

Each of the two detectors contains a 1.8 mm diameter by 60 μm thick silicon wafer. Each detector also has a unique filter foil. This foil screens out lower energy particles and photons that could excite the detector if not blocked. Dosimeter A uses an 18 μm thick aluminum foil, and Dosimeter B uses a 0.2 μm nickel foil.

2. Electrical signal chain

The CuPID dosimeters behave as integral particle detectors with a low voltage reverse bias. The start of a dosimeter count is

when an energetic particle passes the foil and enters the silicon detector. Each energetic particle that passes into or through the detector creates an ionization track of electron-hole pairs. An analog readout of the detector charge is generated using a low-noise charge amplifier ASIC (Application Specific Integrated Circuit). As this readout accumulates over time, the analog to digital converter digitizes the voltage and the FPGA forms data packets for output. Using this circuit method, the instrument produces data in increasing steps of voltage as the dosimeter accumulates charge. Each step is 0.0196 V. Once the charge limit is reached (5.0 V, total 256 steps), the charge is removed, and the increasing steps restart from 0 V. The dosimeter steps are reported as a low count for each small step and a medium count for each rollover count.

To simplify and improve the robustness of the instrument, the dosimeter receives no commanding from the satellite and is designed to only take measurements and output data when powered.

TABLE II. Small particle instruments on CubeSats.

Instrument/CubeSat	Detector Quantity	Energy resolution	Operation duration	Instrument SWAP	FOV	Sample cadence
REPTile/CSSWE	1	Yes	>2 years	1.25 kg, 0.68 W	52°	Event based
MeRIT/CeREs	1	Yes	N/A	1.13 kg, 0.3 W	31 cm ² sr	5 ms–1s
FIRE/FIREBIRD-II	2	Yes	>5 years	1/2U inst.	180° and 45°	18.75 ms
AC6-A and -B	3	No	A-6 years, B-4 years	1/2U s/c	2 at 60°, 1 at 180°	0.1 s
$\mu\text{CPT}/\text{AC10-B}$	1	Yes	>2 years	0.27 kg, 1/4U inst., 0.37 W	48°	2 s (variable)
EPD/ELFIN	2	Yes	>2.5 years	1 kg, 1U inst., 2W	20° and 22°	Event based
Micro-dosimeter/CuPID	2	No	TBD	70 g, 0.33 W	35°	0.1 s

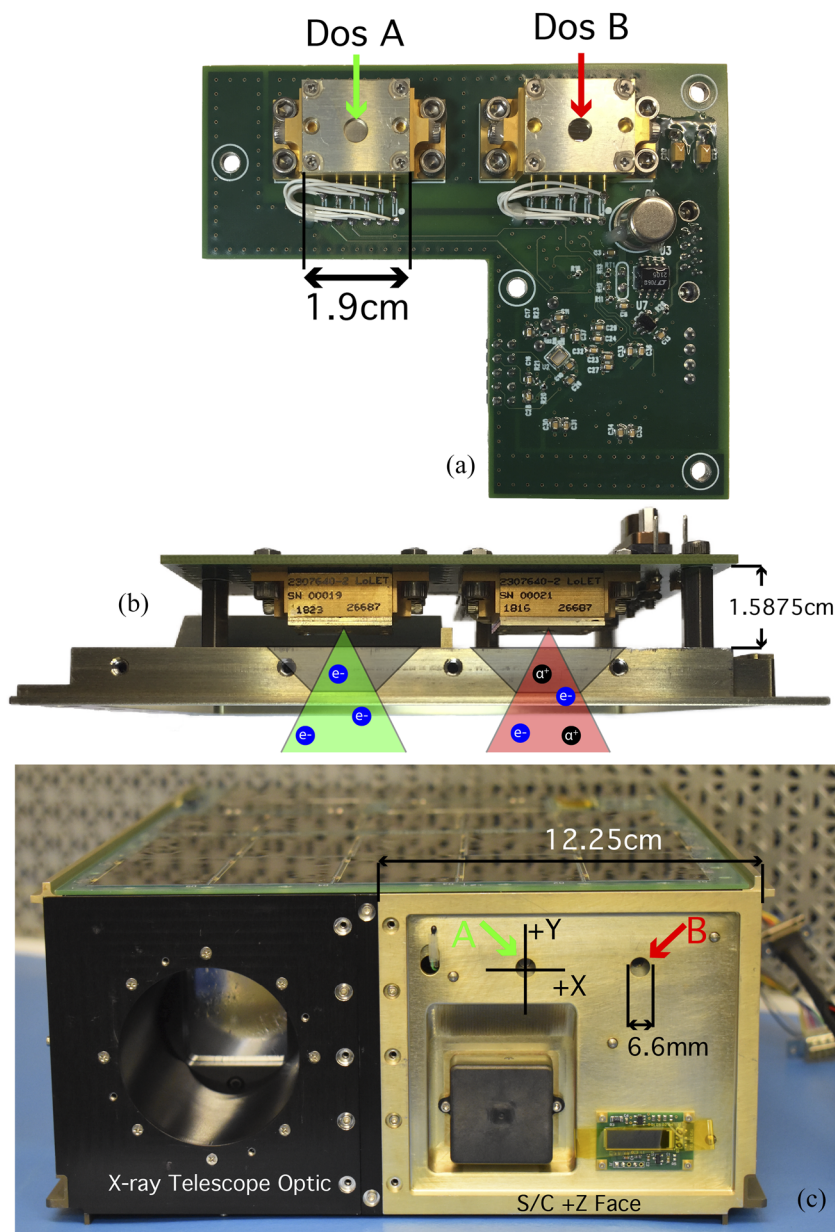


FIG. 12. (a) Micro-dosimeter suite itself with labeled Dos A and Dos B. (b) Top view of the structural endcap mounting with representative apertures and FOV. (c) Front view of the endcap on the CuPID that the suite mounts behind. Included are the axes used for FOV testing. The dosimeter is aligned with the optical axis of the x-ray telescope.

The dosimeter is supplied with 12 V power from the bus, and when operating at room temperatures, the dosimeter consumes 0.028 A. The dosimeter takes measurements of detector charge at 10 Hz, and the FPGA outputs data packets at 1 Hz. Each packet contains a sync word, time stamps of mission elapsed time, voltage monitor data, temperature measurements, and 10 Hz data of the low and medium counts from each detector.

3. Calibration and qualification

The testing of the micro-dosimeter instrument consisted of three experiments to test the FOV, thermal response, and particle

discrimination abilities. The experiment methods were developed on an engineering unit and performed on the flight unit hardware. GEANT4 modeling was conducted to support the laboratory experiments.⁸¹

a. Field-of-View The FOV of the instrument was tested using a small structure to simulate the spacecraft and replicate the flight mounting of the dosimeter. The structure was attached to a rotational shaft inside a vacuum chamber. The instrument was rotated around an axis that bisected the collimating aperture face by a stepper motor that rotated the shaft inside the chamber.

Two perpendicular axes of each detector FOV were tested, shown in Fig. 12(c) where the dosimeter axes match spacecraft axes. Placed inside the chamber with the dosimeter was a fixed radiation source, either Americium 241 (Am241: α , 5.486 MeV) or Strontium 90 (Sr90: β -spectrum, 546 keV maximum with 196 keV average). The instrument was manually calibrated to have its zero angle pointed square with the radiation source. Starting from zero, the instrument was rotated by ± 35 in 1 or 1/2 steps and dwelt 12 min or 3.5 minutes at each step for the Sr90 and Am241 experiments, respectively. The result of dosimeter B testing with Sr90 and Am241 is shown in Fig. 13(a) in comparison to GEANT4 particle simulations. Since FOV testing was conducted at two axes, Fig. 13(b) shows an interpolated polar plot of the FOV where the color map shows normalized counts per second and the radial axes are the angle off of concentric with the detector. From this interpolated plot, it is apparent that the FOV is not concentric with the detector, as seen by the 3° shift toward the upper left. This is due to compounding tolerance build-up in the mounting scheme of the instrument but does not affect the performance of the detector or impact the mission science. A summary of the FOV results is shown in Table III. Dosimeter A was only tested with the Sr90 source because the $18 \mu\text{m}$ aluminum was designed to limit proton measurements.

These experiments determined the FOV to be a maximum of 56° for electrons from the Sr90 source and 40° for protons from the Am241 source and a FWHM near 35° for both particle types.

During nominal science operation, the CuPID will be pointing the dosimeters and x-ray telescope zenith while traveling over Earth's polar regions. In this attitude, the instrument will measure precipitating particles in or near the loss-cone.

b. Detector performance It is well established that silicon detectors perform differently with changes in temperature. To provide a quality on-orbit data product, thermal calibration experiments were performed on the instrument and provide a thermal dependence curve for each detector.

The experiment was conducted inside a thermal chamber where the temperature was stepped from -10 to 60°C in 10°C steps. These temperatures are defined by CuPID's requirements for the instrument. The dosimeter was excited by a Sr90 source, assumed as a constant excitation of the detector. The two detectors were tested independently. Thermocouples were attached to the detector and circuit board to monitor the temperature and provide data to calibrate the temperature sensor in the dosimeter. Figure 14(a) shows the experimental setup before placement inside the thermal chamber. Dosimeter A is covered with the Sr90 source. Figure 14(b) shows the thermal dependence curves. This curve shows that the rate at which energy is deposited in silicon decreases nearly linearly as temperature increases. A linear fit gives an R^2 value of 0.9989 for Dos A and 0.992 for Dos B. The data points were generated by averaging a short period of dosimeter data in stable temperature steps. The count rates between the dosimeters are different because of the different foil filters.

The thermal experiment determined the dependence of the count rate on temperature. On-orbit data will be corrected to room temperature, 23°C , with the known calibration slope. The temperature is determined from a thermal probe included in the dosimeter board and dosimeter telemetry stream.

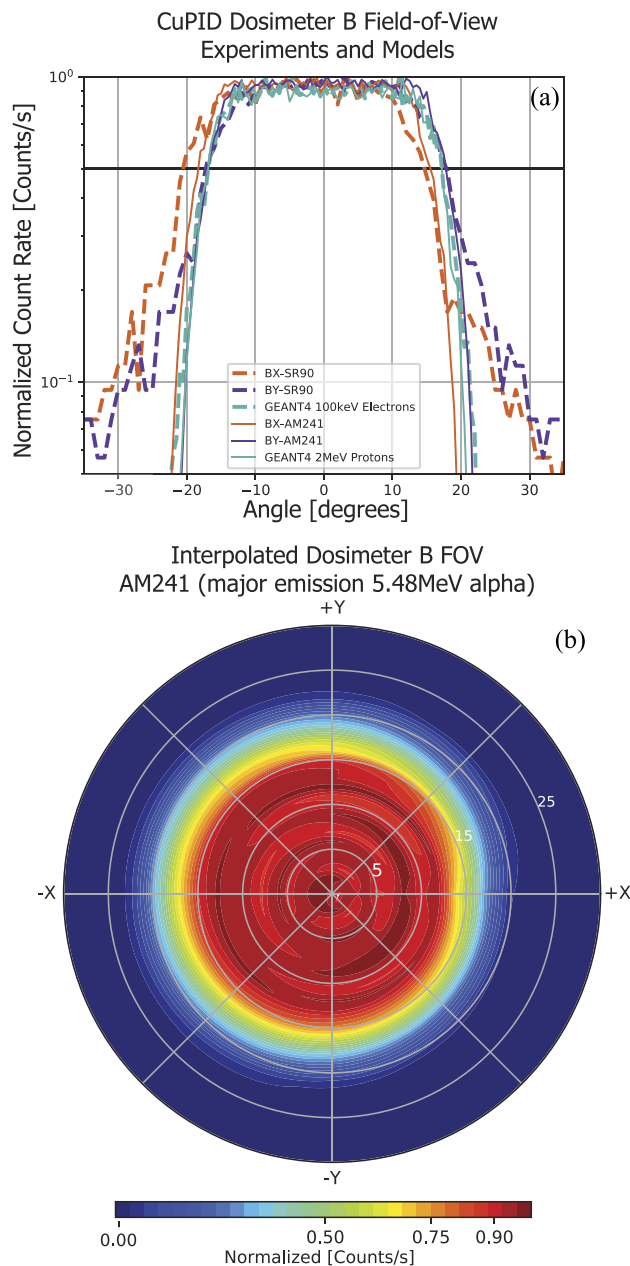


FIG. 13. (a) Summary of the results of dosimeter B FOV experiments with both Sr90 (β) and Am241 (α) radiation sources shown in comparison to GEANT4 simulations of the experiment. The dark horizontal line at $y = 0.5$ is the full width half maximum. (b) Interpolated 2D polar plot of dosimeter B FOV with Am241; radial axes are the spacecraft axes, and angular axes are the degree from the center of the detector.

The third set of experiments conducted on the dosimeter instrument was to determine the detector sensitivity and the discrimination ability of the instruments. The foil thickness was confirmed with a Promethium 147 (Pm147) source that showed higher rates in Dos A (thicker foil) than in Dos B (thinner foil). GEANT4

TABLE III. Results of experimental and modeled FOV.

Experiment	Axis	Source	FOV ^a (deg)
GEANT4	Both	100 keV e-	34
GEANT4	Both	2 MeV α	34
Dos A	X	Sr90	35
Dos A	Y	Sr90	35
Dos B	X	Sr90	36
Dos B	Y	Sr90	35
Dos B	X	Am241	34°
Dos B	Y	Am241	35

^aMeasured as the FWHM of the FOV.

models varied the incident particle energy on the dosimeters and determined the peak response region of the dosimeter. Figures 15(a) and 15(b) show the results of the GEANT4 modeling. The low energy response shows the discrimination accomplished by the foil filters. The peak response, or Bragg peak, shows where a particle is stopped by the total thickness, 60 μm , of silicon. It should be noted that the Bragg peak comes from a combination of losses in the foil filter and silicon. The peak results of Fig. 15(b), dosimeter A, agree with the experimental testing of count rate dependence on electron energy in a beta spectrometer [Fig. 15(d)]. The beam intensity is assumed constant at each energy (i.e., constant source β spectrum). These experiments determined the detector energy response as shown in Table IV. Although the detectors can respond to particle energies below 50 keV, the deposited dose from these low energy particles is not enough to generate counts above that from higher energy particles that are measured at the same time. Due to this response, the effective low energy limit of the dosimeter suite is 50 keV.

Experimental discrimination testing was conducted in a vacuum chamber under high vacuum. The trials included exciting

both detectors with solely the Sr90 source (β -spectrum), solely the Am241 source (α source), and both the Sr90 and Am241 sources simultaneously. Figure 15(c) shows the results of these experiments. The count rate is converted to $\mu\text{Rads/s}$ with a count/ μRads conversion factor that was determined as 270.7 $\mu\text{Rads/count}$ and 343.5 $\mu\text{Rads/count}$ for dosimeters A and B, respectively. These conversion factors were found using calibrated Gadolinium-148 and Curium-244 sources. The alpha particle energy from these sources is propagated through the foil filters, and known source count rates are related to dosimeter count rates. On-orbit, the mission team plans to estimate the ion population by subtracting dosimeter A rates from dosimeter B rates, as shown in the *Ion Comparison* column of Fig. 15(c). This is possible because of the different foil filters. The 3.45% error between the calculated ion population and the actual ion population is because dosimeter A also responds to the Am241 source and particles from radioactive decay are generally a spectrum of energies and species.

The instrument response to varying electron energies was experimentally tested on a beta spectrometer at The Aerospace Corporation. Figure 15(d) shows the dosimeter count rates in comparison to varying electron energies. The electron beam intensity is assumed constant at varying energies (uniform shape β source). The curves are similar when compared to the modeled electron response [Fig. 15(b)]. Dos B shows more sensitivity to lower energies because of the thinner foil. The electron energy of the peak response in Dos A agrees well between the model and experiment near 0.25 MeV.

The dosimeter was also tested against an Fe55 x-ray source (5.9 and 6.5 keV) and to confirm that no counts are generated from x-ray radiation in this energy band.

C. Magnetometer

The CuPID carries a body-mounted RM3100 magneto-inductive magnetometer built by PNI Sensor Corporation, initially

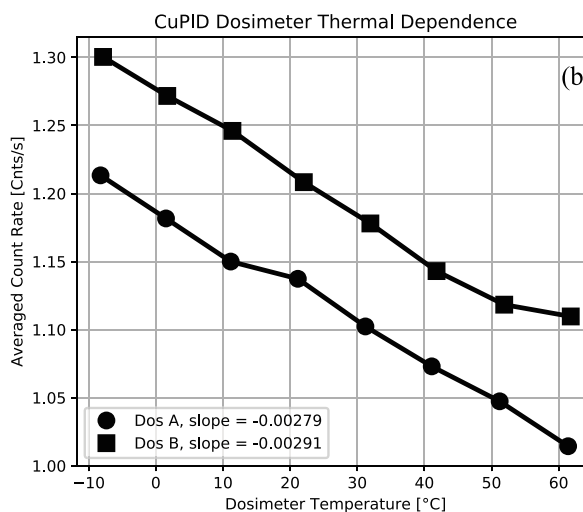
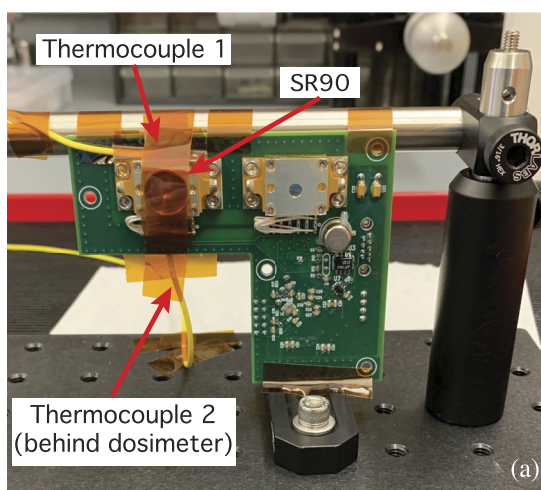


FIG. 14. (a) Dosimeter setup before placement in the thermal chamber with dosimeter A excited by the Sr90 source. Two labeled external thermocouples are used for the calibration. (b) Thermal response of both detectors resulting in $d(\text{Count rate})/d(\text{Temp})$.

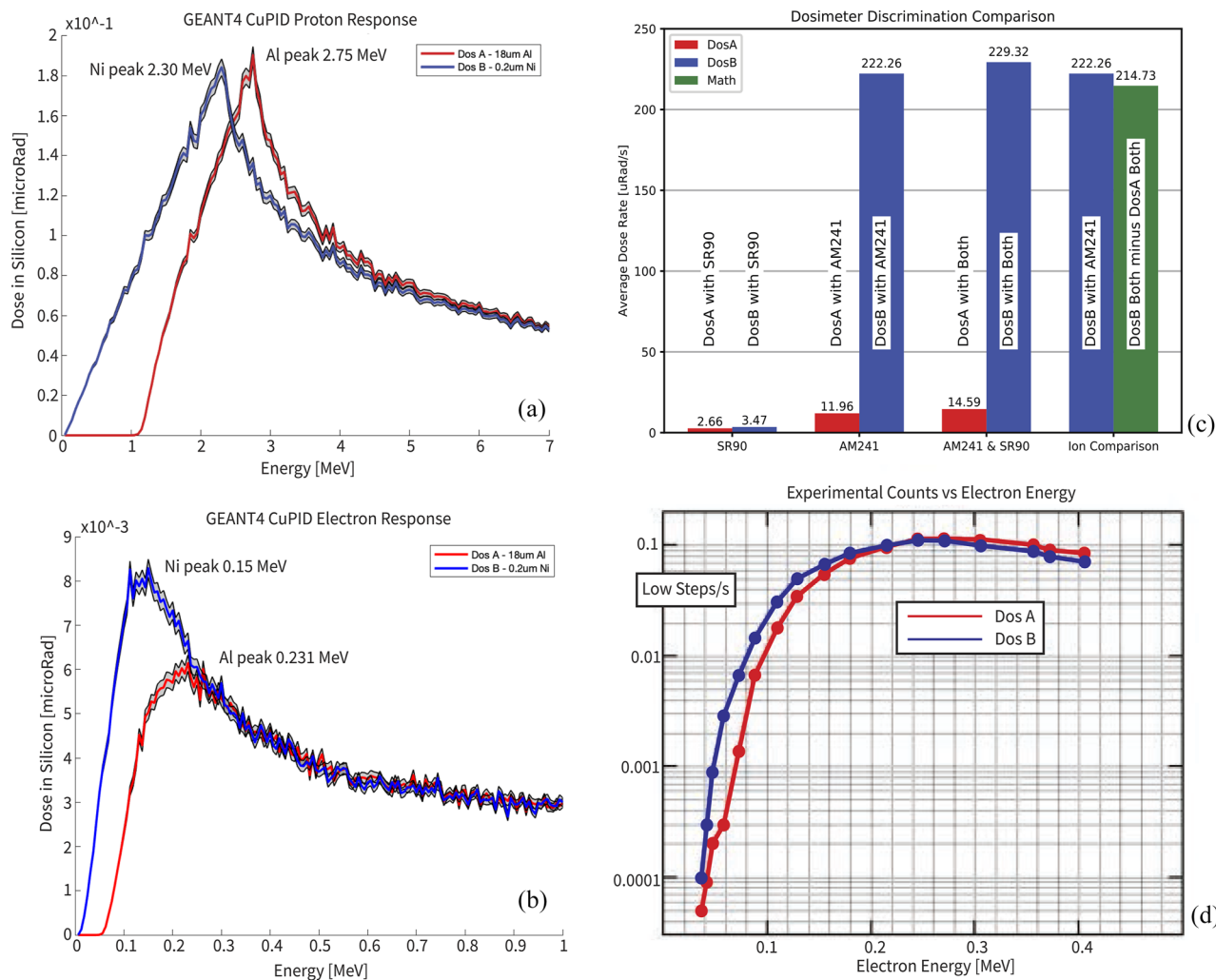


FIG. 15. Modeling and testing of CuPID's dosimeter dependence on particle energy. (a/b) GEANT4 simulations of dose deposited in the detector from energetic particles. The X-axis is the incident particle energy. The RMS error of the Monte Carlo model is shown by the gray bounds. (c) Experimental particle discrimination using Sr90 (beta spectrum, e⁻) and Am241 (α emitter) sources. Three experiments were conducted for each average. The ion comparison bars show the calculated ion population (green) during the Am241 and Sr90 experiments in comparison to the actual ion population, Dos B, Am241 experiment. The calculated ion population is Dos B–Dos A and shows only a 3.45% difference from the actual ion population. (d) Experimental count rate dependence on electron energy in a beta spectrometer.

installed only for spacecraft attitude determination. Magneto-inductive magnetometers are commonly used for small spacecraft avionics systems as engineering magnetometers due to their small size, low cost, and good accuracy for attitude determination systems. However, the unprocessed signal from the CuPID's

magnetometer is insufficient for science measurements for several reasons. The CuPID's magnetometer is mounted directly to the chassis of the spacecraft, which causes the magnetometer to pick up internally generated magnetic fields. These noise components can negatively impact the sensitivity of the instrument, especially to low amplitude signals.⁸² Additionally, at its default sampling rate, the CuPID's magnetometer is accurate to within 50 nT as rated by PNI. This accuracy is low compared to, for example, science grade fluxgate magnetometers that are typically used in the space environment to measure DC magnetic fields. For instance, the fluxgate magnetometers aboard the Magnetospheric Multiscale (MMS) mission spacecraft are accurate to within 0.1 nT.⁸³

TABLE IV. CuPID dosimeter energy.

Detector	Electrons (e ⁻) (keV)	Protons (+)
A	>50	>1 MeV
B	>50	>50 keV

Recently, the utility of body-mounted engineering magnetometers for science applications has begun to be explored, enabled by new robust calibration algorithms. The Active Magnetosphere and Planetary Electrodynamics Response Experiment (AMPERE) mission is an excellent example of this utility, as it consists of a constellation of 75 satellites in the iridium communication network each equipped with a body-mounted engineering magnetometer.^{84,85} Despite the fact that its engineering magnetometers have an accuracy of 30–48 nT and have 10–1000 nT noise contaminants from on-board electronics, measurements from the constellation have proven to be of great utility to those studying ionospheric field aligned currents (FACs).^{86–92} This research was enabled by a series of novel post-processing techniques developed by the AMPERE team to improve the magnetometer data quality, partially consisting of extensive noise identification, attribution, calibration, and correction that produces magnetic field measurements with stability better than 50 nT.⁸² These higher quality measurements are then combined via another post-processing procedure to derive the global distribution of ionospheric currents.⁸⁵ The AMPERE mission sets an excellent example of how to extract maximum utility from engineering magnetometers that have traditionally been considered insufficient for producing scientifically useful measurements. The CuPID's magnetometer faces similar constraints and is therefore developed into a science instrument in a similar manner.

A magnetometer that once was only for navigation now supports the mission with reference magnetic field measurements to constrain the magnetic topology, and cusp regions, through which the CuPID orbits and observes. In addition, the magnetometer is sensitive enough to observe magnetic field reversals of low altitude auroral current sheets. These observations have been previously conducted with CubeSat engineering magnetometers at a 10 second resolution (about 76 km).⁹³ CuPID's 5 s resolution will improve on this measurement, thus providing an opportunity for additional science like its engineering magnetometer predecessors.

1. Mechanical design

The CuPID's magnetometer board is mounted on its avionics package (see Fig. 1, yellow box, and Fig. 16). The bracket that the board is mounted to, while not fully inside the avionics package, is still not electrically isolated from the rest of the chassis and is close to numerous components that generate strong magnetic fields (e.g., battery heater, x-ray board stack, and reaction wheels). This is common for small spacecraft navigation magnetometers and is sufficient for navigation purposes. However, as can be seen in subsequent calibrations (e.g., Fig. 18), this configuration results in the magnetometer picking up noise components generated internally to the spacecraft that can be calibrated out or removed via signal processing to maximize accuracy for scientific measurements. The magnetometer mounting scheme still has some notable advantages. The bracket is mounted as far as possible from the sweeping magnets by the optics of the x-ray telescope, reducing most of the DC field contamination the magnets may cause.

2. Electrical design

In magneto-inductive magnetometers, an oscillating current is applied to the inductor, and the difference between the discharge times of the circuit for each current direction is measured. For zero

applied field, the discharge time in each direction is the same. As a field is applied, the inductance of the inductor becomes different depending on the direction of applied current; therefore, the discharge time of the circuit in each direction will also be different. The difference between the discharge times is directly related to the applied magnetic field.⁹⁴

The CuPID's magnetometer in its default configuration samples the magnetic field in each axis at a rate of 4 Hz (one discharge in each direction). This is considerably lower than the manufacturer's rated maximum of 534 Hz and is sufficient to provide navigation-quality field resolution. The signal from the magnetometer is passed through an analog to digital converter (ADC) and digitized to a bit resolution of 32 nT. The signal is then passed to the avionics system.

The 4 Hz sample rate of the magnetometer is out of phase with the 4 Hz fire rate of magnetorquers. This prevents signals from the largest source of internal magnetic noise to the magnetometer.

3. Calibration and qualification

In order to calibrate and develop a signal processing scheme for the CuPID's magnetometer, the spacecraft was magnetically isolated inside a Helmholtz cage to remove the ambient DC field. Laboratory

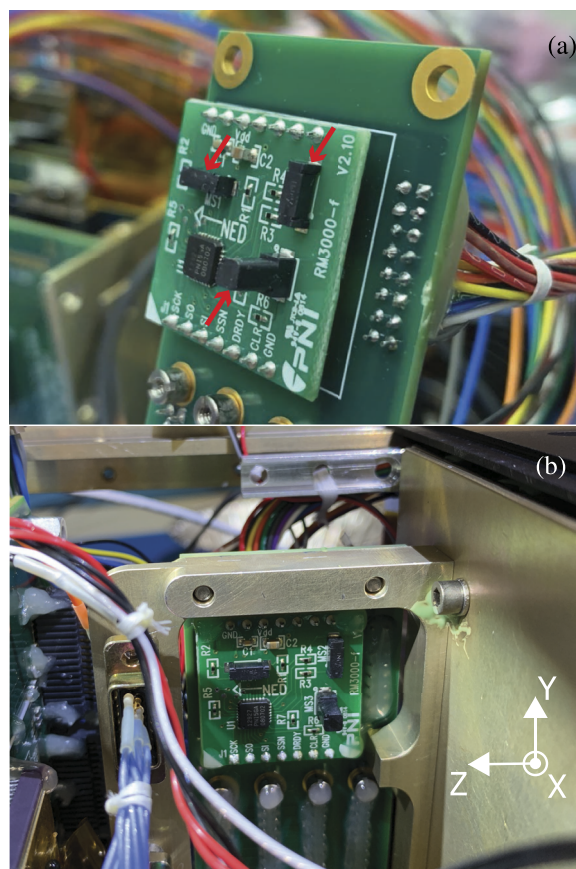


FIG. 16. (a) PNI RM3100 magnetometer. (b) Mounting of the magnetometer inside the CuPID and magnetometer coordinate system.

magnetic noise was not removed. First, a reference magnetometer was placed in the Helmholtz cage without the spacecraft, and the coil field strength varied until the Earth's magnetic field and the magnetic field of the room were completely nullified within the area of the cage. Then, the CuPID was placed at the center of the cage, with the reference fluxgate magnetometer placed as close as possible to the CuPID's magnetometer in order to serve as a reference. This procedure ensures that the only magnetic field components measured using the CuPID's magnetometer are generated by the CuPID itself.

The CuPID's magnetometer is observed to have random noise components roughly 100 nT in amplitude when operating inside CuPID's chassis at its default sampling rate of 4 Hz. In order to improve the accuracy of the measurements and mitigate these random noise components for magnetometer science data,

higher-cadence avionics magnetometer measurements are averaged for five seconds (20 samples at a rate of 4 Hz). This technique has been used to boost the performance of PNI's magneto-inductive chips in previous studies.⁹⁵ To test whether this improved CuPID's magnetometer accuracy and stability, a field was applied to the CuPID using the Helmholtz cage. The field was varied from -1000 to 1000 nT in 100 nT steps (21 steps total) in each axis, with each step being held for three minutes (36 measurements). The field was also measured using a reference magnetometer positioned close to the CuPID's magnetometer. The readings of the CuPID's magnetometer and the reference magnetometer are shown in Fig. 17(a).

Taking a running average of 20 samples mitigates some of the random noise in the CuPID's magnetometer. However, taking the Fourier transform of the signals from each of the magnetometer

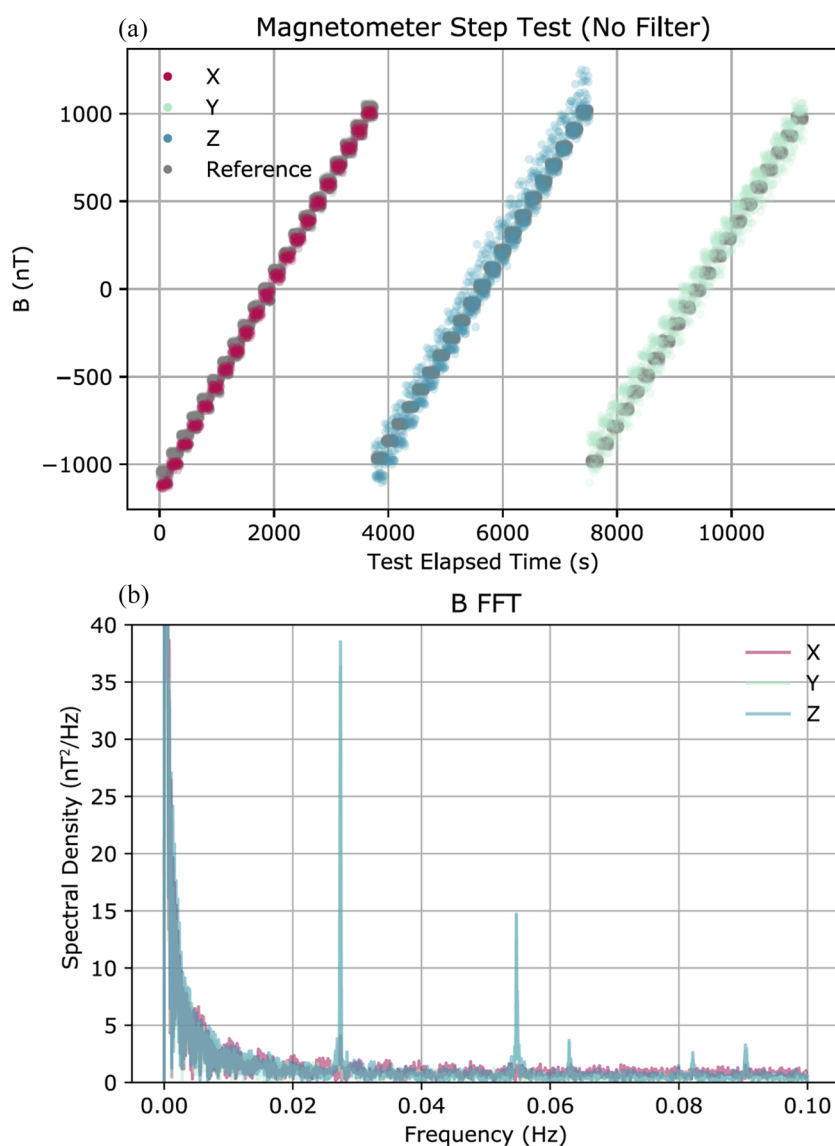


FIG. 17. (a) Readings from the CuPID's magnetometer using the five second averaging technique (shown in red, green, and blue) and readings from the reference magnetometer next to the CuPID's magnetometer. Note that there is some noise in Y and Z channels of the CuPID that is not mitigated by the averaging technique. (b) Fast Fourier Transform (FFT) of the CuPID's magnetometer signal in each channel during the test shown in part A. Note the strong noise components observable at 0.028 Hz and its second and third harmonics and at 0.062 and 0.091 Hz in the Y and Z channels primarily.

channels reveals strong periodic signals, particularly at 0.028 Hz and its second and third harmonics in the Y and Z channels that are not observed in the X channel [see Fig. 17(b)]. One likely source of this noise is the power and data cables running to the CuPID. The cables are oriented in the X direction of the CuPID; therefore, any magnetic field they generate will be the strongest in Y and Z directions of the CuPID. For an experiment with a high requirement for sensitivity, the electrical design could be modified to improve magnetic cleanliness. Since the configuration allows the mission science requirements to be met, the noise is removed in post-processing.

The noise components are periodic; therefore they can be removed by applying filters in frequency space to the signal of the magnetometer.⁸² A targeted set of band pass filters provides adequate noise reduction without much sensitivity cost. Since the Helmholtz cage is not in a vacuum chamber, the CuPID was unable to have the x-ray high voltage powered on. Due to magnetic noise generated by the high voltage power supply, the magnetic noise environment observed here is necessarily different from the one observed on orbit. This means that a targeted set of filters will have to be developed on orbit as opposed to in the lab. However, the performance gains of noise reduction can be tested using a simple low pass filter that cuts out signals above 0.02 Hz applied to the signals from all three magnetometer channels. This filter would render the magnetometer insensitive to magnetic field variations (such as those generated by FACs) smaller than 400 km, unlike several targeted band pass filters. After applying the filter, the performance of the magnetometer is quantified by subtracting the reference field at each step in Fig. 17 from each measurement at that step to obtain the signed variance of each measurement, which then makes a histogram of all the variances and fits a Gaussian to the histogram. The distance of the peak from 0 is a diagnostic of any biases in the measurements, and the width of the Gaussian is a measure of random variance in the measurements. Histograms for each channel before and after the filter are shown in Fig. 18.

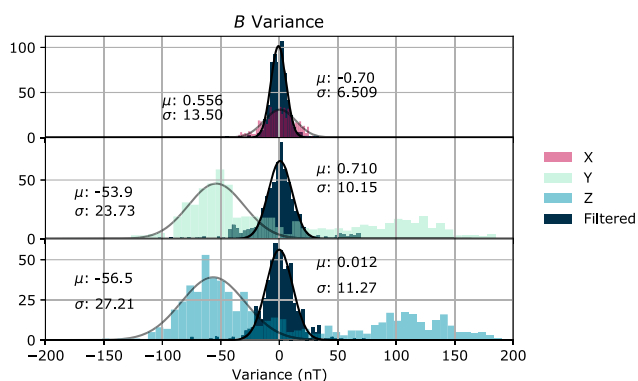


FIG. 18. Histograms of measurement variances in all three magnetometer channels. Colored histograms are unfiltered data (visible in Fig. 17), and black histograms are data with low pass filter applied. Note the strong improvement in accuracy for all three channels after filtering.

Applying a filter to the magnetometer data results in great improvements in measurement accuracy and stability. Prior to filtering, the Y and Z channels consistently measured a -55 nT of field off from the measured applied field and limited the accuracy to within roughly 25 nT. After filtering, the accuracy of all channels is within 12 nT. The factory rated accuracy of this instrument running in its default configuration is 50 nT; the data processing steps developed here have resulted in a five-fold improvement in accuracy. Further refinement of this process on orbit will allow for similar performance with a reduced effect on the instrument sensitivity. As it stands, the combination of averaging many magnetometer samples and then filtering out noise from the resulting signal allows for additional science to be done with the CuPID without the need to develop custom components or add additional loads to CuPID's power or weight budget.

III. SUMMARY

The CuPID CubeSat observatory carries a suite of compact instruments designed for sensitive measurements of solar wind charge exchange and the space environment from a platform in low Earth orbit. The soft x-ray imager utilizes lobster-eye micropore optics to focus soft x rays at a position sensing micro-channel plate detector plane. The system images over a large field of view, $4.6^\circ \times 4.6^\circ$, capturing ion dispersions in the magnetospheric cusp with an angular resolution of 22 arcmin. A micro-dosimeter suite measures energetic particles greater than 50 keV. The instrument is aligned with the FOV of the x-ray telescope and collimated to 35° to measure precipitating particles over the poles. Data from the body-mounted engineering magnetometer have been calibrated, and noise from spacecraft bus signals has been filtered. Measurements from the magnetometer are stored and telemetered to the ground for additional science analysis. Each instrument is designed to be compact and fit into the volume and low resources of a 6U CubeSat. The characterization of the instruments demonstrates a highly capable suite of tools to remotely study the effects of magnetopause reconnection.

ACKNOWLEDGMENTS

The authors would like to thank Michael Collier for his contributions to the micro-pore optic imaging community. His valuable input has helped develop the field to where it is today, and he will be greatly missed. The authors would like to acknowledge the support of J. Estano and B. Sjostrom from BU's EPIC facility for their machining and manufacturing knowledge. Additionally, the CuPID team would like to thank T. Johnson and J. Hudeck of the Small Satellite Project Office, Wallops Flight Facility, for their mission support and guidance. This work was supported by NASA Grant No. NNX16AJ73G, Heliophysics Technology and Instrument Development for Science program.

AUTHOR DECLARATIONS

Conflict of Interest

The authors have no conflicts to disclose.

DATA AVAILABILITY

The data used are available from the corresponding author upon request.

REFERENCES

- ¹J. W. Dungey, "Interplanetary magnetic field and the auroral zones," *Phys. Rev. Lett.* **6**, 47 (1961).
- ²P. A. Cassak, "Inside the black box: Magnetic reconnection and the magnetospheric multiscale mission," *Space Weather* **14**, 186–197, <https://doi.org/10.1002/2015sw001313> (2016).
- ³B. M. Walsh, M. R. Collier, E. Atz, L. Billingsley, J. M. Broll, H. K. Connor, D. Chornay, T. Cragwell, N. Dobson, S. Eckert *et al.*, "The cusp plasma imaging detector (CuPID) CubeSat observatory: Mission overview," *J. Geophys. Res.: Space Phys.* **126**, e2020JA029015, <https://doi.org/10.1029/2020ja029015> (2021).
- ⁴C. T. Russell and R. C. Elphic, "ISEE observations of flux transfer events at the dayside magnetopause," *Geophys. Res. Lett.* **6**, 33–36, <https://doi.org/10.1029/gl006i001p00033> (1979).
- ⁵B. M. Walsh, C. M. Komar, and Y. Pfau-Kempf, "Spacecraft measurements constraining the spatial extent of a magnetopause reconnection X line," *Geophys. Res. Lett.* **44**, 3038–3046, <https://doi.org/10.1002/2017gl073379> (2017).
- ⁶Y. Zou, B. M. Walsh, Y. Nishimura, V. Angelopoulos, J. M. Ruohoniemi, K. A. McWilliams, and N. Nishitani, "Local time extent of magnetopause reconnection using space-ground coordination," *Ann. Geophys.* **37**, 215–234 (2019).
- ⁷Y. Zou, B. M. Walsh, E. Atz, H. Liang, Q. Ma, and V. Angelopoulos, "Azimuthal variation of magnetopause reconnection at scales below an earth radius," *Geophys. Res. Lett.* **47**, e2019GL086500, <https://doi.org/10.1029/2019gl086500> (2020).
- ⁸M. W. Dunlop, Q. H. Zhang, Y. V. Bogdanova, M. Lockwood, Z. Pu, H. Hasegawa, J. Wang, M. G. Taylor, J. Berchem, B. Lavraud *et al.*, "Extended magnetic reconnection across the dayside magnetopause," *Phys. Rev. Lett.* **107**, 025004 (2011).
- ⁹T. Laitinen, M. Palmroth, T. Pulkkinen, P. Janhunen, and H. Koskinen, "Continuous reconnection line and pressure-dependent energy conversion on the magnetopause in a global MHD model," *J. Geophys. Res.: Space Phys.* **112**, A11201, <https://doi.org/10.1029/2007ja012352> (2007).
- ¹⁰T. D. Phan, L. M. Kistler, B. Klecker, G. Haerendel, G. Paschmann, B. U. Ö. Sonnerup, W. Baumjohann, M. B. Bavassano-Cattaneo, C. W. Carlson, A. M. DiLellis *et al.*, "Extended magnetic reconnection at the earth's magnetopause from detection of bi-directional jets," *Nature* **404**, 848 (2000).
- ¹¹B. M. Walsh, J. C. Foster, P. J. Erickson, and D. G. Sibeck, "Simultaneous ground- and space-based observations of the plasmaspheric plume and reconnection," *Science* **343**, 1122–1125 (2014).
- ¹²B. U. Ö. Sonnerup, G. Paschmann, I. Papamastorakis, N. Sckopke, G. Haerendel, S. J. Bame, J. R. Asbridge, J. T. Gosling, and C. T. Russell, "Evidence for magnetic field reconnection at the earth's magnetopause," *J. Geophys. Res.: Space Phys.* **86**, 10049–10067, <https://doi.org/10.1029/ja086ia12p10049> (1981).
- ¹³B. M. Walsh, M. R. Collier, K. D. Kuntz, F. S. Porter, D. G. Sibeck, S. L. Snowden, J. A. Carter, Y. Collado-Vega, H. K. Connor, T. E. Cravens *et al.*, "Wide field-of-view soft X-ray imaging for solar wind-magnetosphere interactions," *J. Geophys. Res.: Space Phys.* **121**, 3353–3361, <https://doi.org/10.1002/2016ja022348> (2016).
- ¹⁴J. L. Burch, T. E. Moore, R. B. Torbert, and B. L. Giles, "Magnetospheric multiscale overview and science objectives," *Space Sci. Rev.* **199**, 5–21 (2016).
- ¹⁵A. Bhardwaj, G. Randall Gladstone, R. F. Elsner, N. Østgaard, J. Hunter Waite, Jr, T. E. Cravens, S.-W. Chang, T. Majeed, and A. E. Metzger, "First terrestrial soft X-ray auroral observation by the chandra X-ray observatory," *J. Atmos. Sol.-Terr. Phys.* **69**, 179–187 (2007).
- ¹⁶P. Sandholt, C. J. Farrugia, J. Moen, and W. Denig, "The cusp in rapid transition," *J. Geophys. Res.: Space Phys.* **107**, SMP-8, <https://doi.org/10.1029/2001ja009214> (2002).
- ¹⁷F. Pitout, C. P. Escoubet, B. Klecker, and H. Rème, "Cluster survey of the mid-altitude cusp: 1. Size, location, and dynamics," *Ann. Geophys.* **24**, 3011–3026 (2006).
- ¹⁸F. Pitout, C. P. Escoubet, B. Klecker, and I. Dandouras, "Cluster survey of the mid-altitude cusp—Part 2: Large-scale morphology," *Ann. Geophys.* **27**, 1875–1886 (2009).
- ¹⁹F. Pitout and Y. Bogdanova, "The polar cusp seen by cluster," *J. Geophys. Res.: Space Phys.* **126**, e2021JA029582, <https://doi.org/10.1029/2021ja029582> (2021).
- ²⁰H. Wolter, "Glancing incidence mirror systems as imaging optics for X-rays," *Ann. Phys.* **445**, 94 (1952).
- ²¹E. Caroli, J. B. Stephen, G. Di Cocco, L. Natalucci, and A. Spizzichino, "Coded aperture imaging in X- and gamma-ray astronomy," *Space Sci. Rev.* **45**, 349–403 (1987).
- ²²C. Winkler, "Integral. The international gamma-ray astrophysics laboratory," *Astron. Astrophys., Suppl. Ser.* **120**, 637–640 (1996).
- ²³N. Gehrels, G. Chincarini, P. e. Giommi, K. Mason, J. Nousek, A. Wells, N. White, S. Barthelmy, D. Burrows, L. Cominsky *et al.*, "The swift gamma-ray burst mission," *Astrophys. J.* **611**, 1005 (2004).
- ²⁴M. Feroci, E. Costa, P. Soffitta, E. Del Monte, G. Di Persio, I. Donnarumma, Y. Evangelista, M. Frutti, I. Lapshov, F. Lazzarotto *et al.*, "SuperAGILE: The hard X-ray imager for the AGILE space mission," *Nucl. Instrum. Methods Phys. Res., Sect. A* **581**, 728–754 (2007).
- ²⁵N. Østgaard, J. E. Balling, T. Bjørnsen, P. Brauer, C. Budtz-Jørgensen, W. Bujwan, B. Carlson, F. Christiansen, P. Connell, C. Eyles *et al.*, "The modular X- and gamma-ray sensor (MXGS) of the ASIM payload on the international space station," *Space Sci. Rev.* **215**, 1–28 (2019).
- ²⁶R. A. Marshall, W. Xu, T. Woods, C. Cully, A. Jaynes, C. Randall, D. Baker, M. McCarthy, H. E. Spence, G. Berland *et al.*, "The AEPEX mission: Imaging energetic particle precipitation in the atmosphere through its bremsstrahlung X-ray signatures," *Adv. Space Res.* **66**, 66–82 (2020).
- ²⁷M. J. Cieślak, K. A. Gamage, and R. Glover, "Coded-aperture imaging systems: Past, present and future development—A review," *Radiat. Meas.* **92**, 59–71 (2016).
- ²⁸J. Wang and Y. Zhao, "Snr of the coded aperture imaging system," *Opt. Rev.* **28**, 106–112 (2021).
- ²⁹G. Branduardi-Raymont, S. F. Sembay, J. P. Eastwood, D. G. Sibeck, T. A. Abbey, P. Brown, J. A. Carter, C. M. Carr, C. Forsyth, D. Kataria *et al.*, "AXIOM: Advanced X-ray imaging of the magnetosphere," *Exp. Astron.* **33**, 403–443 (2012).
- ³⁰C. H. Feldman, R. Willingale, J. Pearson, V. Aslanyan, T. Crawford, P. Houghton, J. Sykes, C. Bicknell, J. Osborne, P. O'Brien *et al.*, "Calibration of a fully populated lobster eye optic for SVOM," in *Space Telescopes and Instrumentation 2020: Ultraviolet to Gamma Ray* (International Society for Optics and Photonics, 2020), Vol. 11444, p. 114441K.
- ³¹R. Hudec, "Kirkpatrick-Baez (KB) and lobster eye (LE) optics for astronomical and laboratory applications," *X-Ray Opt. Instrum.* **2010**, 139148.
- ³²A. G. Peele, K. A. Nugent, A. V. Rode, K. Gabel, M. C. Richardson, R. Strack, and W. Siegmund, "X-ray focusing with lobster-eye optics: A comparison of theory with experiment," *Appl. Opt.* **35**, 4420–4425 (1996).
- ³³R. Willingale, J. Pearson, A. Martindale, C. Feldman, R. Fairbend, E. Schyns, S. Petit, J. Osborne, and P. O'Brien, "Aberrations in square pore micro-channel optics used for x-ray lobster eye telescopes," in *Space Telescopes and Instrumentation 2016: Ultraviolet to Gamma Ray* (International Society for Optics and Photonics, 2016), Vol. 9905, p. 99051Y.
- ³⁴K. D. Kuntz, E. Atz, M. R. Collier, Y. Collado-Vega, H. K. Connor, F. S. Porter, D. G. Sibeck, and B. M. Walsh, "Making the invisible visible: X-ray imaging," in *Magnetospheric Imaging* (Elsevier, 2022), pp. 59–99.
- ³⁵M. Galeazzi, M. R. Collier, T. Cravens, D. Koutroumpa, K. D. Kuntz, S. Lepri, D. McCammon, F. S. Porter, K. Prasai, I. Robertson *et al.*, "Solar wind charge exchange and local hot bubble x-ray emission with the DXL sounding rocket experiment," *Astron. Nachr.* **333**, 383–387 (2012).
- ³⁶M. R. Collier, F. S. Porter, D. G. Sibeck, J. A. Carter, M. P. Chiao, D. J. Chornay, T. E. Cravens, M. Galeazzi, J. W. Keller, D. Koutroumpa *et al.*, "Invited article: First flight in space of a wide-field-of-view soft x-ray imager using lobster-eye optics: Instrument description and initial flight results," *Rev. Sci. Instrum.* **86**, 071301 (2015).
- ³⁷E. J. Bunce, A. Martindale, S. Lindsay, K. Muinonen, D. A. Rothery, J. Pearson, I. McDonnell, C. Thomas, J. Thornhill, T. Tikkanen *et al.*, "The BepiColombo mercury imaging x-ray spectrometer: Science goals, instrument performance and operations," *Space Sci. Rev.* **216**, 126 (2020).

- ³⁸N. E. Thomas, J. A. Carter, M. P. Chiao, D. J. Chornay, Y. M. Collado-Vega, M. R. Collier, T. E. Cravens, M. Galeazzi, D. Koutroumpa, J. Kujawski, *et al.*, “The DXL and STORM sounding rocket mission,” in *UV, X-Ray, and Gamma-Ray Space Instrumentation for Astronomy XVIII* (International Society for Optics and Photonics, 2013), Vol. 8859, p. 88590Z.
- ³⁹W. Raab, G. Branduardi-Raymont, C. Wang, L. Dai, E. Donovan, G. Enno, P. Escoubet, A. Holland, L. Jing, D. Kataria *et al.*, “Smile: A joint ESA/CAS mission to investigate the interaction between the solar wind and earth’s magnetosphere,” in *Space Telescopes and Instrumentation 2016: Ultraviolet to Gamma Ray* (International Society for Optics and Photonics, 2016), Vol. 9905, p. 990502.
- ⁴⁰G. W. Fraser, J. D. Carpenter, D. A. Rothery, J. F. Pearson, A. Martindale, J. Huovelin, J. Treis, M. Anand, M. Anttila, M. Ashcroft *et al.*, “The mercury imaging x-ray spectrometer (MIXS) on bepicolombo,” *Planet. Space Sci.* **58**, 79–95 (2010).
- ⁴¹A. Martindale, J. Pearson, G. Fraser, J. Carpenter, R. Willingale, T. Stevenson, C. Whitford, F. Giannini, R. Fairbend, J. Seguy *et al.*, “The mercury imaging x-ray spectrometer: Optics design and characterisation,” in *Instruments and Methods for Astrobiology and Planetary Missions XII* (International Society for Optics and Photonics, 2009), Vol. 7441, p. 744117.
- ⁴²J. Trümper, “The ROSAT mission,” *Adv. Space Res.* **2**, 241–249 (1982).
- ⁴³K. Mitsuda, M. Bautz, H. Inoue, R. L. Kelley, K. Koyama, H. Kunieda, K. Makishima, Y. Ogawara, R. Petre, T. Takahashi, *et al.*, “The x-ray observatory Suzaku,” *Publ. Astron. Soc. Jpn.* **59**, S1–S7 (2007).
- ⁴⁴D. N. Burrows, J. E. Hill, J. A. Nousek, J. A. Kennea, A. Wells, J. P. Osborne, A. F. Abbey, A. Beardmore, K. Mukerjee, A. D. T. Short *et al.*, “The swift X-ray telescope,” *Space Sci. Rev.* **120**, 165–195 (2005).
- ⁴⁵F. Jansen, D. Lumb, B. Altieri, J. Clavel, M. Ehle, C. Erd, C. Gabriel, M. Guainazzi, P. Gondoin, R. Much, *et al.*, “XMM-Newton observatory-I. The spacecraft and operations,” *Astron. Astrophys.* **365**, L1–L6 (2001).
- ⁴⁶G. P. Garmire, M. W. Bautz, P. G. Ford, J. A. Nousek, and G. R. Ricker, Jr., “Advanced ccd imaging spectrometer (ACIS) instrument on the chandra X-ray observatory,” in *X-Ray and Gamma-Ray Telescopes and Instruments for Astronomy* (International Society for Optics and Photonics, 2003), Vol. 4851, pp. 28–44.
- ⁴⁷N. Thomas, “The STORM and CuPID soft X-ray cameras on the DXL sounding rocket mission: Employment of slumped micropore optics to image solar wind charge exchange X-ray emission in the magnetosheath,” in *AGU Fall Meeting Abstracts* (AGU, 2016), pp. SM33B–2512.
- ⁴⁸D. G. Sibeck, R. Allen, H. Aryan, D. Bodewits, P. Brandt, G. Branduardi-Raymont, G. Brown, J. A. Carter, Y. Collado-Vega, M. R. Collier *et al.*, “Imaging plasma density structures in the soft X-rays generated by solar wind charge exchange with neutrals,” *Space Sci. Rev.* **214**, 79 (2018).
- ⁴⁹A. Caspi, T. N. Woods, and H. P. Warren, “New observations of the solar 0.5–5 keV soft x-ray spectrum,” *Astrophys. J. Lett.* **802**, L2 (2015).
- ⁵⁰C. S. Moore, A. Caspi, T. N. Woods, P. C. Chamberlin, B. R. Dennis, A. R. Jones, J. P. Mason, R. A. Schwartz, and A. K. Tolbert, “The instruments and capabilities of the miniature x-ray solar spectrometer (MinXSS) CubeSats,” *Solar Phys.* **293**, 21–40 (2018).
- ⁵¹S. L. Snowden, R. Egger, M. J. Freyberg, D. McCammon, P. P. Plucinsky, W. T. Sanders, J. H. M. M. Schmitt, J. Trümper, and W. Voges, “Rosat survey diffuse x-ray background maps. II,” *Astrophys. J.* **485**, 125 (1997).
- ⁵²K. D. Kuntz, Y. M. Collado-Vega, M. R. Collier, H. K. Connor, T. E. Cravens, D. Koutroumpa, F. S. Porter, I. P. Robertson, D. G. Sibeck, S. L. Snowden *et al.*, “The solar wind charge-exchange production factor for hydrogen,” *Astrophys. J.* **808**, 143 (2015).
- ⁵³H. Connor, D. Sibeck, M. Collier, I. Baliukin, G. Branduardi-Raymont, P. Brandt, N. Buzulukova, Y. Collado-Vega, C. Escoubet, M.-C. Fok *et al.*, “Soft X-ray and ENA imaging of the earth’s dayside magnetosphere,” *J. Geophys. Res.: Space Phys.* **126**, e2020JA028816, <https://doi.org/10.1029/2020ja028816> (2021).
- ⁵⁴J. Bailey and M. Gruntman, “Experimental study of exospheric hydrogen atom distributions by lyman-alpha detectors on the TWINS mission,” *J. Geophys. Res.: Space Phys.* **116**, A09302, <https://doi.org/10.1029/2011ja016531> (2011).
- ⁵⁵B. M. Walsh, J. Niehof, M. R. Collier, D. T. Welling, D. G. Sibeck, F. S. Mozer, T. A. Fritz, and K. D. Kuntz, “Density variations in the earth’s magnetospheric cusps,” *J. Geophys. Res.: Space Phys.* **121**, 2131–2142, <https://doi.org/10.1002/2015ja022095> (2016).
- ⁵⁶O. H. W. Siegmund, D. E. Everman, J. V. Vallerger, and M. Lampton, “Soft x-ray and extreme ultraviolet quantum detection efficiency of potassium bromide photocathode layers on microchannel plates,” *Appl. Opt.* **27**, 1568–1573 (1988).
- ⁵⁷O. H. W. Siegmund, S. Clothier, J. Thornton, J. Lemen, R. Harper, I. M. Mason, and J. L. Culhane, “Application of the wedge and strip anode to position sensing with microchannel plates and proportional counters,” *IEEE Trans. Nucl. Sci.* **30**, 503–507 (1983).
- ⁵⁸O. H. W. Siegmund, M. Lampton, J. Bixler, S. Chakrabarti, J. Vallerger, S. Bowyer, and R. F. Malina, “Wedge and strip image readout systems for photon-counting detectors in space astronomy,” *J. Opt. Soc. Am. A* **3**, 2139–2145 (1986).
- ⁵⁹C. Martin, P. Jelinsky, M. Lampton, R. F. Malina, and H. O. Anger, “Wedge-and-strip anodes for centroid-finding position-sensitive photon and particle detectors,” *Rev. Sci. Instrum.* **52**, 1067–1074 (1981).
- ⁶⁰J. O. Goldsten, R. H. Maurer, P. N. Peplowski, A. G. Holmes-Siedle, C. C. Herrmann, and B. H. Mauk, “The engineering radiation monitor for the radiation belt storm probes mission,” *The Van Allen Probes Mission* (Springer, 2012), pp. 485–502.
- ⁶¹R. Maurer, J. Goldsten, P. Peplowski, A. Holmes-Siedle, M. Butler, C. Herrmann, and B. H. Mauk, “Early results from the engineering radiation monitor (ERM) and solar cell monitor on the Van Allen probes mission,” *IEEE Trans. Nucl. Sci.* **60**, 4053–4058 (2013).
- ⁶²X. Li, Q. Schiller, L. Blum, S. Califf, H. Zhao, W. Tu, D. L. Turner, D. Gerhardt, S. Palo, S. Kanekal *et al.*, “First results from CSSWE CubeSat: Characteristics of relativistic electrons in the near-earth environment during the October 2012 magnetic storms,” *J. Geophys. Res.: Space Phys.* **118**, 6489–6499, <https://doi.org/10.1002/2013ja019342> (2013).
- ⁶³A. Breneman, A. Crew, J. Sample, D. Klumpar, A. Johnson, O. Agapitov, M. Shumko, D. Turner, O. Santolik, J. R. Wygant *et al.*, “Observations directly linking relativistic electron microbursts to whistler mode chorus: Van Allen probes and FIREBIRD II,” *Geophys. Res. Lett.* **44**, 11–265, <https://doi.org/10.1002/2017gl075001> (2017).
- ⁶⁴A. B. Crew, H. E. Spence, J. B. Blake, D. M. Klumpar, B. A. Larsen, T. P. O’Brien, S. Driscoll, M. Handley, J. Legere, S. Longworth *et al.*, “First multipoint in situ observations of electron microbursts: Initial results from the NSF FIREBIRD II mission,” *J. Geophys. Res.: Space Phys.* **121**, 5272–5283, <https://doi.org/10.1002/2016ja022485> (2016).
- ⁶⁵B. R. Anderson, S. Shekhar, R. M. Millan, A. B. Crew, H. E. Spence, D. M. Klumpar, J. B. Blake, T. P. O’Brien, and D. L. Turner, “Spatial scale and duration of one microburst region on 13 August 2015,” *J. Geophys. Res.: Space Phys.* **122**, 5949–5964, <https://doi.org/10.1002/2016ja023752> (2017).
- ⁶⁶L. W. Blum, Q. Schiller, X. Li, R. Millan, A. Halford, and L. Woodger, “New conjunctive CubeSat and balloon measurements to quantify rapid energetic electron precipitation,” *Geophys. Res. Lett.* **40**, 5833–5837, <https://doi.org/10.1002/2013gl058546> (2013).
- ⁶⁷M. Shumko, J. Sample, A. Johnson, B. Blake, A. Crew, H. Spence, D. Klumpar, O. Agapitov, and M. Handley, “Microburst scale size derived from multiple bounces of a microburst simultaneously observed with the FIREBIRD-II CubeSats,” *Geophys. Res. Lett.* **45**, 8811–8818, <https://doi.org/10.1029/2018gl078925> (2018).
- ⁶⁸M. Shumko, A. T. Johnson, J. G. Sample, B. A. Griffith, D. L. Turner, T. P. O’Brien, O. Agapitov, J. B. Blake, and S. G. Claudepierre, “Electron microburst size distribution derived with AeroCube-6,” *J. Geophys. Res.: Space Phys.* **125**, e2019JA027651, <https://doi.org/10.1029/2019JA027651> (2020).
- ⁶⁹M. Shumko, A. T. Johnson, T. P. O’Brien, D. L. Turner, A. D. Greeley, J. G. Sample, J. B. Blake, L. W. Blum, and A. J. Halford, “Statistical properties of electron curtain precipitation estimated with AeroCube-6,” *J. Geophys. Res.: Space Phys.* **125**, e2020JA028462, <https://doi.org/10.1029/2020JA028462> (2020).
- ⁷⁰K. Zhang, X. Li, Q. Schiller, D. Gerhardt, H. Zhao, and R. Millan, “Detailed characteristics of radiation belt electrons revealed by CSSWE/REPtile measurements: Geomagnetic activity response and precipitation observation,” *J. Geophys. Res.: Space Phys.* **122**, 8434–8445, <https://doi.org/10.1002/2017ja024309> (2017).
- ⁷¹L. Capannolo, W. Li, H. Spence, A. Johnson, M. Shumko, J. Sample, and D. Klumpar, “Energetic electron precipitation observed by FIREBIRD-II potentially driven by EMIC waves: Location, extent, and energy range from a multievent analysis,” *Geophys. Res. Lett.* **48**, e2020GL091564, <https://doi.org/10.1029/2020gl091564> (2021).

- ⁷²J. F. Fennell, J. B. Blake, S. Claudepierre, J. Mazur, S. Kanekal, P. O'Brien, D. Baker, W. Crain, D. Mabry, and J. Clemmons, "Current energetic particle sensors," *J. Geophys. Res.: Space Phys.* **121**, 8840–8858, <https://doi.org/10.1002/2016ja022588> (2016).
- ⁷³D. Gerhardt, S. Palo, X. Li, L. Blum, Q. Schiller, and R. Kohnert, The Colorado Student Space Weather Experiment (CSSWE) On-Orbit Performance, 2013.
- ⁷⁴S. G. Kanekal, L. Blum, E. R. Christian, G. Crum, M. Desai, J. Dumonthier, A. Evans, A. D. Greeley, S. Guerro, S. Livi *et al.*, "The MERIT onboard the CeREs: A novel instrument to study energetic particles in the earth's radiation belts," *J. Geophys. Res.: Space Phys.* **124**, 5734–5760, <https://doi.org/10.1029/2018ja026304> (2019).
- ⁷⁵H. E. Spence, J. Blake, A. Crew, S. Driscoll, D. Klumpar, B. Larsen, J. Legere, S. Longworth, E. Mosleh, T. O'Brien, *et al.*, "Focusing on Size and Energy dependence of electron microbursts from the Van Allen radiation belts," *Space Weather* **10** (2012).
- ⁷⁶J. B. Blake and T. P. O'Brien, "Observations of small-scale latitudinal structure in energetic electron precipitation," *J. Geophys. Res.: Space Phys.* **121**, 3031–3035, <https://doi.org/10.1002/2015ja021815> (2016).
- ⁷⁷V. Angelopoulos, E. Tsai, L. Bingley, C. Shaffer, D. L. Turner, A. Runov, W. Li, J. Liu, A. V. Artemyev, X. J. Zhang *et al.*, "The elfin mission," *Space Sci. Rev.* **216**, 103 (2020).
- ⁷⁸D. L. Turner, J. H. Lee, C. Q. Nguyen, W. R. Crain, Jr., A. L. Berman, and J. B. Blake, "The micro-charged particle telescope (μ CPT) for the AeroCube-10 mission," in *AGU Fall Meeting Abstracts* (AGU, 2018), Vol. 2018, pp. SH41D–3669.
- ⁷⁹C. Wilkins, R. Caron, V. Angelopoulos, P. R. Cruce, M. Chung, J. Liu, A. Runov, K. Rowe, E. Tsai, and L. Bingley, "Calibration and first-light of the energetic particle detectors on UCLA's electron losses and fields investigation (ELFIN) CubeSats," in *AGU Fall Meeting Abstracts* (AGU, 2018), Vol. 2018, pp. SH41D–3668.
- ⁸⁰S. L. O'Dell, M. W. Bautz, W. C. Blackwell, Jr., Y. M. Butt, R. A. Cameron, R. F. Elsner, M. S. Gussenhoven, J. J. Kolodziejczak, J. I. Minow, R. M. Suggs *et al.*, "Radiation environment of the Chandra X-ray observatory," in *X-ray and Gamma-Ray Instrumentation for Astronomy XI* (International Society for Optics and Photonics, 2000), Vol. 4140, pp. 99–110.
- ⁸¹S. Agostinelli, J. Allison, K. Amako, J. Apostolakis, H. Araujo, P. Arce, M. Asai, D. Axen, S. Banerjee, G. Barrand *et al.*, "Geant4—A simulation toolkit," *Nucl. Instrum. Methods Phys. Res., Sect. A* **506**, 250–303 (2003).
- ⁸²B. J. Anderson, S. K. Vines, C. L. Waters, and R. J. Barnes, "Finally! AMPERE-next-it's about TIME (thermosphere-ionosphere-magnetosphere electrodynamics)," in *AGU Fall Meeting Abstracts* (AGU, 2020), Vol. 2020, p. SA022–0003.
- ⁸³C. T. Russell, B. J. Anderson, W. Baumjohann, K. R. Bromund, D. Dearborn, D. Fischer, G. Le, H. K. Leinweber, D. Leneman, W. Magnes *et al.*, "The magnetospheric multiscale magnetometers," *Space Sci. Rev.* **199**, 189–256 (2016).
- ⁸⁴B. J. Anderson, K. Takahashi, and B. A. Toth, "Sensing global Birkeland currents with iridium[®] engineering magnetometer data," *Geophys. Res. Lett.* **27**, 4045–4048, <https://doi.org/10.1029/2000gl000094> (2000).
- ⁸⁵B. Anderson, J. Gjerloev, C. Waters, H. Korth, L. Dyrud, and R. Barnes, "Night-time transient Birkeland currents observed by AMPERE," in *AGU Fall Meeting Abstracts* (AGU, 2010), Vol. 2010, p. SM41C–1888.
- ⁸⁶C. L. Waters, B. J. Anderson, and K. Liou, "Estimation of global field aligned currents using the iridium[®] system magnetometer data," *Geophys. Res. Lett.* **28**, 2165–2168, <https://doi.org/10.1029/2000gl012725> (2001).
- ⁸⁷B. Anderson, K. Takahashi, T. Kamei, C. Waters, and B. Toth, "Birkeland current system key parameters derived from iridium observations: Method and initial validation results," *J. Geophys. Res.: Space Phys.* **107**, SMP–11, <https://doi.org/10.1029/2001ja000080> (2002).
- ⁸⁸H. Korth, B. J. Anderson, M. J. Wiltberger, J. G. Lyon, and P. Anderson, "Intercomparison of ionospheric electrodynamics from the iridium constellation with global MHD simulations," *J. Geophys. Res.: Space Phys.* **109**, A07307, <https://doi.org/10.1029/2004ja010428> (2004).
- ⁸⁹L. Clausen, J. Baker, J. Ruohoniemi, S. Milan, and B. Anderson, "Dynamics of the region 1 Birkeland current oval derived from the active magnetosphere and planetary electrodynamics response experiment (AMPERE)," *J. Geophys. Res.: Space Phys.* **117**, A06233, <https://doi.org/10.1029/2012ja017666> (2012).
- ⁹⁰F. Wilder, G. Crowley, B. Anderson, and A. Richmond, "Intense day-side joule heating during the 5 April 2010 geomagnetic storm recovery phase observed by AMIE and AMPERE," *J. Geophys. Res.: Space Phys.* **117**, A05207, <https://doi.org/10.1029/2011ja017262> (2012).
- ⁹¹S. Marsal, A. Richmond, A. Maute, and B. Anderson, "Forcing the TIEGCM model with Birkeland currents from the active magnetosphere and planetary electrodynamics response experiment," *J. Geophys. Res.: Space Phys.* **117**, A06308, <https://doi.org/10.1029/2011ja017416> (2012).
- ⁹²V. G. Merkin, B. J. Anderson, J. G. Lyon, H. Korth, M. Wiltberger, and T. Motoba, "Global evolution of Birkeland currents on 10 min timescales: MHD simulations and observations," *J. Geophys. Res.: Space Phys.* **118**, 4977–4997, <https://doi.org/10.1002/jgra.50466> (2013).
- ⁹³J. B. Parham, V. Beukelaers, L. Leung, J. Mason, B. Walsh, and J. Semeter, "Leveraging commercial CubeSat constellations for auroral science: A case study," *J. Geophys. Res.: Space Phys.* **124**, 3487–3500, <https://doi.org/10.1029/2018ja025966> (2019).
- ⁹⁴A. Leuzinger and A. Taylor, "Magneto-inductive technology overview," PNI white paper, 2010.
- ⁹⁵L. H. Regoli, M. B. Moldwin, M. Pellioni, B. Bronner, K. Hite, A. Sheinker, and B. M. Ponder, "Investigation of a low-cost magneto-inductive magnetometer for space science applications," *Geosci. Instrum., Methods Data Syst.* **7**, 129–142 (2018).